

1 **Imprint of minute hydrocarbon seepage on solid phase and pore water**
2 **geochemistry in organic-poor subseafloor sediment**

3 Ellen Schnabel^{1*}, Jessica Stammeier², Stefanie Poetz³, Kai Mangelsdorf³, Aurèle Vuillemin¹,
4 Rolando di Primio⁴, Jens Kallmeyer¹, the PROSPECTOMICS Consortium

5 ¹GFZ Helmholtz Centre for Geosciences, Section Geomicrobiology, Telegrafenberg, 14473
6 Potsdam, Germany

7 ²GFZ Helmholtz Centre for Geosciences, Section Inorganic and Isotope Geochemistry,
8 Telegrafenberg, 14473 Potsdam, Germany

9 ³GFZ Helmholtz Centre for Geosciences, Section Organic Geochemistry, Telegrafenberg,
10 14473 Potsdam, Germany

11 ⁴AkerBP, 1366 Lysaker, Norway

12 *Corresponding author: MSc Ellen Schnabel, eschnabe@gfz.de

13 Keywords: hydrocarbon seepage; reductive diagenesis; authigenic minerals; microbial
14 activity; Barents Sea; sediment biogeochemistry

15 **Key Points**

- 16 • Even inconspicuous hydrocarbon seepage in organic-poor sediments modifies redox
17 zonation, highlighting previously unrecognized biogeochemical sensitivity in low-flux
18 systems.
- 19 • Subtle seepage causes distinct spatial heterogeneity in pore water chemistry and
20 mineral formation patterns.
- 21 • Authigenic minerals and pore water gradients serve as complementary indicators of
22 past and ongoing seepage.

23 **Abstract**

24 In marine environments, small hydrocarbon (HC) fluxes through organic-poor sediments are
25 often fully degraded by microorganisms before reaching the seabed. Yet, these fluxes
26 influence sediment geochemistry by stimulating microbial activity. We analyzed 50 gravity
27 cores from the southwestern Barents Sea, covering zones affected by inconspicuous HC
28 seepage and unaffected reference zones. Using various organic and inorganic geochemical

29 analyses of the sediment along with pore water geochemistry, we assess the effects of low-
30 intensity seepage and identify potential geochemical signatures.

31 While analysis of the organic geochemical analyses provided limited insights, inorganic
32 geochemical analyses revealed formation of minerals such as carbonates and sulfides, linked
33 to microbial reductive processes. Element concentrations suggested that HC degradation
34 leaves distinct signatures, particularly in redox-sensitive minerals. Pore water profiles in HC-
35 affected zones showed significant variation, indicating carbonate precipitation. In contrast,
36 sediments not affected by HC seepage displayed more uniform pore water profiles.

37 Estimated fluxes of sulfate, calcium, and alkalinity varied notably between cores, particularly
38 in HC-affected zones, suggesting local and potentially transient differences in seepage
39 intensity.

40 While microbial HC degradation likely occurs deeper than our sampling interval, high-
41 resolution geochemical analysis of both sediment fractions and pore water revealed a clear
42 imprint of HC seepage. This imprint, reflected in authigenic minerals and pore water
43 gradients, allows identification of past and present seepage activity, with authigenic
44 minerals providing evidence for past seepage, and pore water profiles informing about
45 ongoing seepage.

46 **Plain language summary**

47 Hydrocarbons like methane or oil can naturally seep from underground reservoirs into
48 marine sediments. Often, this seepage is so small that hydrocarbons are fully degraded by
49 microorganisms before they reach the upper sediment layers near the seafloor.

50 In this study, we analyzed sediment from the southwestern Barents Sea, a region with very
51 low natural organic content, to investigate whether such subtle hydrocarbon seepage leaves
52 detectable traces, even when hydrocarbons are already consumed below the depth we
53 sampled.

54 Our results show that despite the complete degradation of hydrocarbons deeper in the
55 sediment, distinct changes in pore water chemistry and mineral composition persist in the
56 upper layers. We observed variations in sulfate, calcium, and alkalinity profiles, along with
57 the formation of minerals like carbonates and sulfides.

58 These findings reveal that even low-intensity hydrocarbon seepage can leave a long-lasting
59 imprint in sediments, not only through direct hydrocarbon presence, but also through their
60 impact on geochemical processes. This insight helps improving the detection of past or
61 ongoing seepage in marine environments and supports a better understanding of
62 biogeochemical cycles below the seafloor.

63 **1. Introduction**

64 Marine subseafloor biogeochemical cycles are primarily governed by microorganisms (Joye
65 et al., 2022), their metabolic activity is strongly controlled by availability and reactivity of
66 sedimentary organic substrates. Due to lesser primary productivity of surface waters as
67 compared to coastal areas (Chavez et al., 2011), in offshore sediments bioavailable organic
68 matter (OM) is typically limited and becomes more recalcitrant with burial depth
69 (Middelburg, 2018) due to lower sedimentation rates (Røy et al., 2012). However, as all
70 hydrocarbon reservoirs leak to some degree (Hunt, 1995; Heggland, 1998; Yergin, 2009),
71 underlying hydrocarbon reservoirs will lead to buoyant hydrocarbon-rich fluids migrating
72 upwards through the sediment column (Ciotoli et al., 2020). These HCs, even in trace
73 amounts, represent an additional electron donor that can significantly fuel microbial activity
74 (Zhang et al., 2022). Such influx of labile OM (i.e. seepage) leads to changes in microbial
75 communities in terms of diversity and activity, which affect in turn specific physicochemical
76 properties of the sediment, such as porosity, density, pore water geochemistry and mineral
77 composition, (Abrams, 2005; Hvoslef et al., 1996; Joye, 2020). HC seepage through marine
78 sediments fuels a variety of microbial processes, including sulfate reduction, fermentation,
79 and methanogenesis (Joye, 2020; Schnabel et al., 2025). Although these microbial processes
80 are central to *in situ* biogeochemical transformations of OM on the continental shelf
81 (Bradley et al., 2020), they are less pronounced in pelagic sediments wherein sulfate
82 reduction becomes limited due to energy limitation (Vuillemin et al., 2020). Thus, at sites
83 with low seepage rates HCs may be fully mineralized before reaching the sediment surface.
84 Nevertheless, subtle but continuous HC fluxes influence sediment geochemistry and
85 microbiology, not only in the direct vicinity of the HC source but also extending to the
86 sediment surface (Rasheed et al., 2013; Joye et al., 2004).

87 Dissimilatory sulfate reduction (DSR), which is the predominant terminal electron-accepting
 88 pathway in oxygen-depleted, sulfate-containing shallow marine sediments (Kasten and
 89 Jørgensen, 2000; Bowles et al., 2014; Jørgensen et al., 2019), can be expected to be
 90 influenced by HC seepage and potentially be key in defining HC-related reductive diagenesis
 91 (Joye et al., 2004). Organoclastic sulfate reduction (OSR) relies on low molecular weight
 92 substrates derived from fermented particulate or dissolved OM (Jørgensen, 1982), whereas
 93 methanotrophic sulfate reduction is performed in conjunction with methane-oxidizing
 94 archaea (ANME) during anaerobic oxidation of methane (AOM) (Orphan et al., 2001). Thus,
 95 the influence of HC seepage on sulfate-reducing bacteria (Widdel et al., 2010) highly
 96 depends on whether light (i.e. gaseous, soluble) or heavy (i.e. long chain alkanes, aromatic
 97 rings) HCs are supplied. The types of seeping HCs and their subsequent microbial alteration
 98 can be resolved using mass spectrometry of sediment organic extracts, e.g. a shift from
 99 polar to less polar unsaturated HCs is observed during maturation (Hu et al., 2023), whereas
 100 the loss of hydrogen atoms in alkanes (via dehydrogenation) or oxygen incorporation in
 101 aromatic rings (cleavage via hydroxylation) reveal subsequent microbial alteration (Sert et
 102 al., 2020). Further geochemical effects inherent to sulfate reduction (SR) include an increase
 103 in pore water alkalinity, primarily as dissolved inorganic carbon (DIC) in the form of
 104 bicarbonate (HCO_3^-), and production of hydrogen sulfide (H_2S). Together these metabolic
 105 solutes create favorable sedimentary conditions for the precipitation of carbonate and
 106 sulfide minerals (Berner, 1981; Hinrichs et al., 1999; Lin et al., 2016), namely calcite (CaCO_3),
 107 mackinawite (FeS) and pyrite (FeS_2). Carbonates can record redox conditions at the time of
 108 formation (Vuillemin et al., 2023a and 2023b) while their trace element compositions can
 109 indicate progressive alteration or diagenesis (Smrzka et al., 2019), in particular redox-
 110 sensitive trace metals (Smrzka et al., 2020; Tribovillard et al., 2013). Similarly, iron sulfides
 111 scavenge specific trace elements from the pore water (Huerta-Diaz and Morse, 1992),
 112 including chalcophilic and redox-sensitive bioessential metals (e.g., Mn, Mo, Cu, Zn).

113 Local redox conditions mediated by microbial processes also affect HC mobility as they
 114 promote the formation (e.g. carbonates) or dissolution (e.g. clays) of mineral barriers that
 115 adsorb HCs or impede their diffusion (Zhao et al., 2024; Eichhubl et al., 2009). For instance,
 116 the transition of smectite to illite decreases the mineral swelling capacity and reduces
 117 permeability (Kim et al., 2004; Dong et al., 2009). Such interplay of physical, geochemical

118 and biological factors affects the migration of HCs and generates complex but characteristic
 119 flow patterns at active seep systems (De Groot et al., 2024). Thus, seep systems are
 120 characterized by pronounced spatial and temporal variations, permeability, fluid flow
 121 dynamics, and pressure conditions governing the rate at which HCs migrate upward (Foster
 122 et al., 2015; Leifer et al., 2004; De Groot et al., 2024), reasons for which characteristic HC
 123 seeps can be classified according to flux and surface manifestations (Table 1). Note that
 124 some seep-features like e.g. carbonate crusts or pockmarks remain even after active
 125 seepage stopped (Nickel et al. 2012, Nickel et al. 2013).

126 **Table 1.** Classification of hydrocarbon seeps based on methane flux and associated surface manifestations. The
 127 table is compiled after (Judd and Hovland (2009); Etiope (2015)). The flux range between inconspicuous- and
 128 moderate-flux seeps ($1 \text{ mmol} \times \text{m}^2 \times \text{d}^{-1}$ to $100 \text{ mmol} \times \text{m}^2 \times \text{d}^{-1}$) represents a conceptual transition zone,
 129 where current data are insufficient to establish a clear distinction.

Seep type	Inconspicuous seeps	Moderate seeps	High flux seeps
Flux range	$< 1 \text{ mmol} \times \text{m}^2 \times \text{d}^{-1}$	$0.1\text{--}1 \text{ mol} \times \text{m}^2 \times \text{d}^{-1}$	$1\text{--}10 \text{ mol} \times \text{m}^2 \times \text{d}^{-1}$
Pockmarks	No pockmarks	Small, less deeply pronounced pockmarks	Larger, deeper and more numerous pockmarks, clearer
Methane and gas bubbles	No bubbles	Few, smaller bubbles, mostly sporadic	Frequent and larger bubbles, continuous gas flow
Chemical changes	No or minimal chemical changes on the surface	Low concentration of carbonates and sulfides	Significant enrichment of carbonates and sulfides, possible mineral deposits
Biogenic hotspots	No biological hotspots	Local colonization of methane-oxidizing bacteria	Intensive biological activity, larger hotspots with more diverse methane-fed fauna (e.g. mussels)
Gas hydrates	No gas hydrates	Little or no gas hydrates	Possible presence of gas hydrates, especially at low temperatures and high methane flow

130 According to our definition inconspicuous HC seeps are seeps where the seeping HCs lack
131 visible surface manifestations. Instead, the HCs spread diffusely and are used up by
132 biogeochemical processes so that the HCs do not reach the SWI. Although they likely imprint
133 sediment geochemistry, they often remain undetected. Yet, any additional energy flux from
134 weak seepage tends to promote complex interactions among local microbial communities
135 adapted to substrate limitation or not, and influence the sediment geochemical dynamics,
136 leading to fundamental metabolic and diagenetic processes (Abrams, 2020).

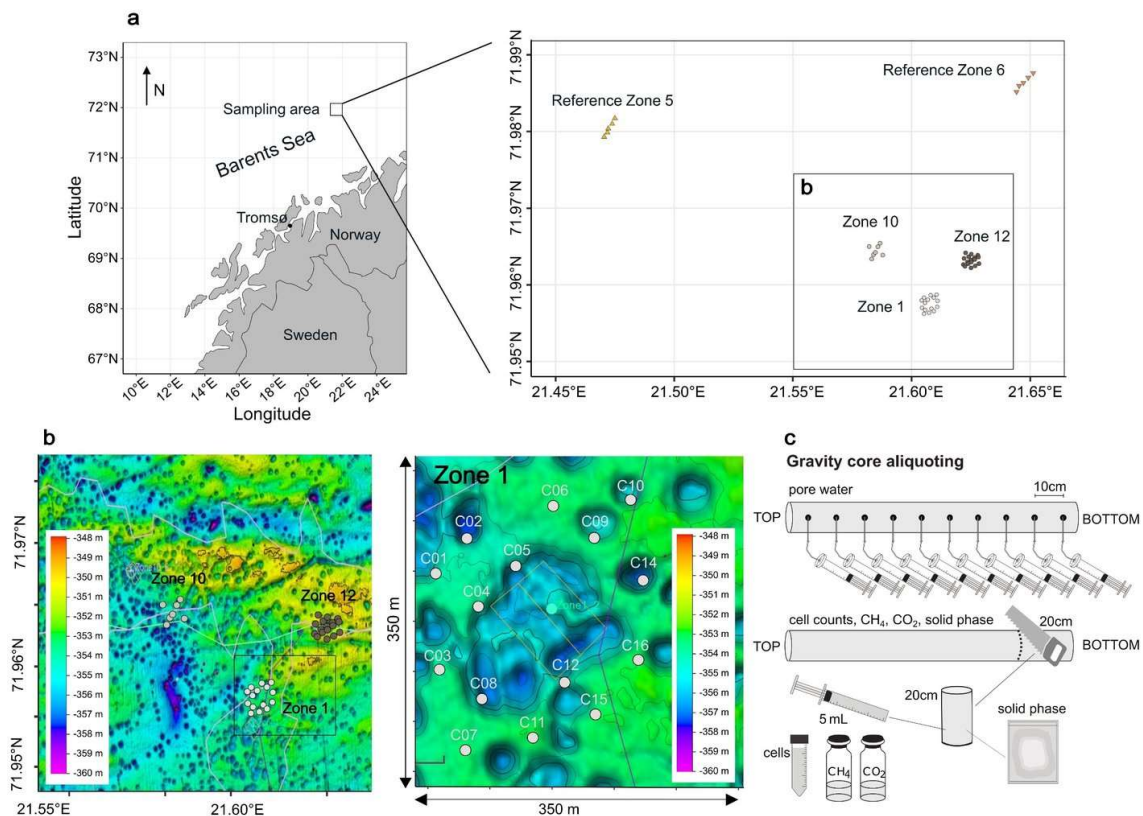
137 Here, we investigate how subtle, inconspicuous HC seepage influences the geochemical
138 composition of both pore water and sediment. We analyzed 50 gravity cores collected from
139 the southwestern Barents Sea, including 40 cores from zones affected by low-intensity
140 seepage and 10 from unaffected reference zones. Given the challenges of deeper coring and
141 the goal of minimizing environmental impact, we focused on the upper 3 meters of
142 sediment to determine whether direct or indirect effects of seepage could be detected. The
143 large number of cores allows us to identify small-scale geochemical patterns and evaluate
144 any spatial heterogeneity of discrete infiltrations. By combining organic and inorganic
145 analyses of the sediment with pore water geochemistry, we decipher (I) the extent to which
146 inconspicuous HC seeps affect the distribution of key geochemical species (e.g. sulfide,
147 methane, calcium, alkalinity) in pore water and sediment, and (II) how these parameters
148 vary spatially across and between seepage and reference zones.

149 **2. Material and Methods**

150 **2.1. Geological setting and sampling**

151 The Barents Sea is an epicontinental shelf sea bordered by the Norwegian Sea to the
152 southwest, the Arctic Ocean to the north, and the Russian archipelago of Novaya Zemlya to
153 the east. It rests on a Caledonian basement formed during Paleozoic orogenies, but its
154 present structural configuration mainly reflects Mesozoic and Cenozoic tectonic phases,
155 including episodes of uplift, subsidence, tilting, and erosion. This has resulted in a varied
156 structural landscape with elevated highs (e.g., the Loppa High) and intervening sedimentary
157 basins (Doré, 1995; Gabrielsen et al., 1990; Johansen et al., 1993; Larssen et al., 2002;
158 Faleide et al., 1984). During the Mesozoic, organic-rich marine shales were deposited under

159 greenhouse climate conditions with high marine productivity and fluctuating sea levels.
 160 These shales—particularly the Upper Jurassic Hekkingen Formation, act as the principal
 161 source rocks for hydrocarbons in the southwestern Barents Sea (Marín et al., 2020; Langrock
 162 et al., 2003). Burial over millions of years led to thermal maturation, hydrocarbon
 163 generation, and subsequent migration into structural traps, such as those found in the
 164 Johan Castberg and Snøhvit fields. In the Quaternary, the region was repeatedly covered by
 165 ice sheets. During the last glaciation, the Barents Sea was overridden by grounded ice,
 166 leading to significant glacial erosion. Consequently, the modern sediment cover on
 167 structural highs is often very thin and sediments primarily consist of glacial and glaciomarine
 168 silty clays, dropstones, and fine sands derived from the erosion of local and distal bedrock
 169 during glacial advance and retreat. These surficial sediments are typically organic-poor,
 170 reflecting both their glacial origin and limited biological productivity during deposition
 171 (Knies and Martinez, 2009; Nickel et al., 2013; Sættem et al. (1991); Elverhøi and Solheim
 172 (1983).



173
 174 **Figure 1. Sampling locations.** (a) Map of the Norwegian coast. The square marks the sampling area. Fifty cores
 175 were retrieved from three HC-affected zones (Zone 1, Zone 10, Zone 12) and two reference zones (Ref 5, Ref
 176 6). (b) Bathymetric map of the 3 HC-affected zones. Each zone was sampled in a grid of cores, Zone 1 is

177 enlarged here as an example. The missing samples in the middle are due to the increased occurrence of
 178 dropstones in this area, preventing the deployment of a gravity corer. (c) Schematic overview of the sampling
 179 strategy. This figure was modified after (Schnabel et al., 2025)

180 During an expedition to the SW Barents Sea in Oct/Nov 2021, we collected a total of fifty
 181 gravity cores, ranging from 0.5 to 3 meters in length, within three zones with known
 182 underlying HC reservoirs (Z01, Z10, Z12), as well as two zones (Ref5, Ref6) with no HC
 183 reservoirs, labelled hereafter as HC zones and reference zones (Fig. 1a). The coring sites lie
 184 at a water depth of approximately 350 meters (Fig. 1b). Immediately after retrieval of a
 185 core (Fig. 1c), the lowermost 20 cm of the core were cut off, the sediment was pushed out
 186 of the liner and the outer 1-2 cm were scraped off with a sterile spatula to remove possible
 187 contamination. Using 5 mL cut-off syringes, 3 cm³ of sediment were transferred into a 10 mL
 188 glass crimp vial containing saturated NaCl solution. The vials were immediately sealed with
 189 thick butyl rubber stoppers, crimped, and stored upside down without headspace until gas
 190 analyses in the home lab. An additional 2 cm³ of sediment was transferred into a 15 mL
 191 centrifuge tube containing 8 mL of NaCl-formalin fixative solution (25 g × L⁻¹ NaCl, 20 g × L⁻¹
 192 formalin) and thoroughly homogenized for cell counting. The remaining sediment was
 193 aliquoted for solid phase geochemistry. The rest of the core was cut into 1 m sections,
 194 capped and stored on deck, as air, water and sediment temperature were all around 5 °C.

195 Pore water was extracted on board, with extractions initiated within two hours of core
 196 retrieval. Rhizon pore water samplers (Rhizosphere Research Products B.V., Netherlands;
 197 (Seeberg-Elverfeldt et al., 2005)) were inserted into the intact sediment core through small
 198 holes drilled in ca. 10 cm intervals. Pore water collection took between 12 and 24 hours. The
 199 collected pore water samples were 0.22 µm- filtered (Merck Millex™-GS Sterile Syringe Filter
 200 Unit, MCE) and aliquoted for different downstream analyses. For anion, cation, and trace
 201 element measurements, 1.5 mL each was collected in plastic screw-cap vials without any
 202 further treatment. These samples were kept anoxic until analysis. For alkalinity
 203 measurements, 2 mL of pore water were filled into a glass vial pre-filled with 50 µL of
 204 saturated HgCl₂ solution to prevent bacterial activity (Edenborn et al., 1985) and closed
 205 without any headspace. For quantification of dissolved hydrogen sulfide, we transferred 1.5
 206 mL of pore water into a 2 mL plastic screw-cap vial and added 200 µL ZnCl₂ (20 % weight ×
 207 vol⁻¹). All samples were stored at +4 °C until analysis in the home lab.

208 2.2. Methane and carbon dioxide concentrations

209 Prior to measurement, we introduced 3 mL of ultrapure helium gas as headspace while
210 withdrawing the same amount of NaCl solution from the crimped vial. To equilibrate
211 dissolved gases with the headspace, the content of the vials was mixed at 220 rpm on an
212 orbital shaker for 18 h, and further vortexed to break up the remaining small clayey
213 aggregates. A 250 μL sample of the headspace gas was then extracted and introduced into a
214 7890A Gas Chromatography System, which was equipped with both a flame ionization
215 detector (FID) and a thermal conductivity detector (TCD), along with an HP PLOT Q column
216 (all from Agilent). The oven temperature was set to 50 $^{\circ}\text{C}$, the flow rate was maintained at
217 17.2 mL min^{-1} , and the pressure was held at 13 psi. Both detectors operated at 200 $^{\circ}\text{C}$ with
218 flow rates of 40 mL min^{-1} (FID) and 15 mL min^{-1} (TCD). Calibration of the system was
219 performed by injecting pure analytical standards with CO_2 concentrations of 310 ppm and
220 5270 ppm, as well as CH_4 concentrations of 10 ppm and 5170 ppm. The initial CH_4 and CO_2
221 concentrations were converted from ppm to molar concentrations using the ideal gas law.

222 2.3. Cell counting

223 Total cell counts were conducted following a protocol based on Kallmeyer et al. (2008).
224 Sediment samples were initially diluted at a ratio of 1:100 using a 25 g L^{-1} NaCl solution. 25
225 μL of the resulting slurry were uniformly distributed onto black 0.2 μm polycarbonate
226 Cyclopore membrane filters (Whatman International Ltd, Maidstone, UK) via vacuum
227 filtration. For cell visualization, filters were stained with a mixture consisting of SYBR Green I
228 (10 μL ; Molecular Probes, Eugene, USA), phenylenediamine (100 μL), glycerol (300 μL), Milli-
229 Q water (300 μL), and 300 μL of VECTASHIELD[®] Antifade Mounting Medium (H-1000-10,
230 Vector Laboratories, Burlingame, USA). A volume of 15 μL of this staining solution was
231 applied to each filter. The counting was performed using an epifluorescence microscope
232 (Leica DM2000, Wetzlar, Germany) by counting cells in 200 fields of view. Cell abundances
233 were calculated as \log_{10} cells per cm^3 of sediment, based on triplicate measurements, with
234 standard deviations consistently remaining below 15%.

235 2.4. Pore water geochemistry

236 Dissolved sulfate was quantified via suppressed Ion Chromatography (column: SykroGel A ×
237 300 AB-A01; eluent: 7.3 mg L⁻¹ NaSCN and 636 mg L⁻¹ NaCO₃; pump rate 1 mL min⁻¹;
238 injection volume 50 μL). The detection limit was 5 μM. Samples were measured in triplicate,
239 with average relative standard deviations consistently below 3%.

240 Cation and trace elemental concentrations in the pore water were determined using high-
241 resolution inductively coupled plasma mass spectrometry (HR-ICP-MS, ELEMENT 2XR,
242 Thermo Scientific, Waltham, USA) at the EIMiE-labs at GFZ after acidifying the samples with
243 ultrapure HNO₃ **immediately prior to analysis**. Until analysis, the samples were kept anoxic
244 to prevent precipitation and potential alteration of the metal concentrations. 100 μL of pore
245 water was doped with 10 μL of an indium (In) standard solution at a concentration of 100
246 μg L⁻¹ and the samples were diluted with 2 vol% ultrapure HNO₃. Trace elements were
247 quantified by external calibration using single-element standards, carefully matched to the
248 sample matrix. The acid blank was subtracted from each measurement. The detection limits
249 for the applied ICP-MS routine typically ranged between 0.5 and 1 ng g⁻¹, for the analytes.
250 Measurement uncertainty, referring to the repeatability of the measurements, was about 2-
251 5 % for all analyses.

252 Iron concentrations were analyzed separately using spectrophotometry, following the
253 protocol described by Viollier et al. (2000). The detection limit of this method is 0.25 μM
254 and the measurement uncertainty was approximately 5 % for all analyses. Sulfide was
255 determined photometrically according to Cline (1969). The detection limit is 0.1 μM. All
256 samples were measured in triplicates and the results were averaged with a standard
257 deviation ≤ 3.5 %. Alkalinity was determined via titration using the Visocolor HE alkalinity AL
258 7 kit (Macherey-Nagel GmbH) adapted to the sample volume of 500 μL. The detection limit
259 is 0.15 mM and triplicate measurements differed by less than 3 %.

260 **2.5. Sediment inorganic fraction**

261 For XRF analysis, approximately 30 g of sediment material was freeze-dried, ground in agate
262 mortars using a Fritsch Pulverisette 5 planetary mill at 300 rpm for 5 minutes, sieved
263 through a 63 μm stainless steel mesh, and then melted with two Fluxana reference
264 materials to form glass discs. These discs were analyzed using an AXIOS X-ray fluorescence

265 (XRF) advanced spectrometer (Malvern Panalytical, United Kingdom), equipped with an End-
 266 window RH X-ray tube SST-mAX at a 4 kW output. Elemental proportions were determined
 267 for major elements as oxides in weight % [wt %] (i.e. SiO₂, Al₂O₃, Fe₂O₃, MnO, MgO, CaO,
 268 Na₂O, K₂O, P₂O₅, TiO₂, SO₃, loss on ignition (LOI)), and trace elements [ppm] (i.e. Ba, Cr, Zn,
 269 Ga, Nb, Ni, Rb, Sr, V, Y, Zr). Quantification limits for major elements were 0.02 wt % and
 270 approximately 10 ppm for trace elements. LOI was determined based on the mass
 271 difference before and after fusion. Reproducibility was evaluated using reference materials
 272 and better than 2% for all major elements.

273 **2.6. Statistical and geostatistical analyses**

274 Min-max normalization was applied to the XRF dataset, scaling all variables to a range
 275 between 0 and 1. PCA was then performed using the `prcomp()` function in R with centering
 276 and scaling enabled to identify patterns and relationships among chemical species in the
 277 solid sediment phase, reducing the data's dimensionality and highlighting key variability
 278 across samples. This analysis provided further insight into the underlying structure of the
 279 data, complementing the subsequent visualizations. For ternary visualization, selected
 280 standardized parameters were then proportionally scaled to sum to 100 %. In some cases,
 281 the resulting values of multiple compounds (e.g., those associated with specific mineral
 282 groups like carbonates) were summed. Thus, the ternary diagrams reflect only relative
 283 patterns and should not be interpreted in terms of absolute abundances.

284 We applied Mann–Whitney U tests (Mann and Whitney, 1947) using the function
 285 `wilcox.test()` to XRF and pore water data to assess whether the median values of individual
 286 chemical species differed significantly between groups. This non-parametric test was used
 287 to evaluate differences in concentration gradients in the pore water and absolute
 288 concentrations in the solid sediment phase between HC-affected zones (Z01, Z10, Z12) and
 289 reference sites (Ref5, Ref6), as well as among and within individual zones and sediment
 290 cores. To assess differences in variability (i.e. variance), we also used the Brown-Forsythe
 291 test (Brown and Forsythe, 1974) applying the `leveneTest()` function . This test allowed us to
 292 assess whether the variance in chemical species concentrations - reflecting chemical
 293 heterogeneity - varied significantly between zones. Finally, Pearson correlation analyses
 294 (Pearson, 1895; Sedgwick, 2012) were conducted on the pore water data to explore linear

295 relationships among chemical species. Two analytical levels were considered: (1)
296 correlations within individual sediment cores, and (2) correlations across all cores from the
297 same sampling zone (e.g., all cores from Z01). All statistical and geostatistical analyses were
298 performed using R version 4.2.0 (R Core Team, 2022).

299 Diffusive fluxes of sulfate, alkalinity, and calcium across the sediment–water interface were
300 calculated based on Fick's first law of diffusion using the linear concentration gradients.
301 Molecular diffusion coefficients were taken from Schulz (2006) and subsequently adjusted
302 for sediment conditions following Iversen and Jørgensen (1993). To visualize spatial patterns
303 in fluxes of sulfate, alkalinity, and calcium, we applied ordinary kriging using the `gstat`
304 package in R (Pebesma, 2004). First, empirical variograms were calculated from spatially
305 referenced flux measurements. Several theoretical variogram models (spherical,
306 exponential, Gaussian, and Matérn) were fitted and compared. The best-fitting model was
307 selected based on convergence criteria and plausibility of the sill and range parameters. This
308 model was then used to interpolate flux values across a regular spatial grid covering the
309 study area. The resulting kriging maps (Matheron, 1963) provided continuous spatial
310 representations of flux gradients and enabled the identification of heterogeneities between
311 hydrocarbon seep zones and reference sites. Visualizations were created using the `ggplot2`
312 package (Wickham, 2016).

313 **2.7. Sediment organic fraction**

314 Molecular-level insights into the organic geochemistry of sediments were obtained for
315 solvent-extractable OM using Fourier Transform Ion Cyclotron Resonance Mass
316 Spectrometry (FT-ICR-MS). Based on geochemical pore water profiles, a subset of 11
317 representative samples consisting of three samples from each of the three HC zones (Z01,
318 Z10, Z12) and one sample from each of the two reference zones (Ref5, Ref6) was selected
319 from the total of 50 sediment cores. For each sample, approximately 10 g of sediment were
320 freeze-dried, milled, and the organic content was extracted using a Soxhlet extractor
321 following a procedure described by Poetz et al. (2014). The extraction was performed with a
322 solvent mixture composed of dichloromethane and methanol (v/v = 99:1) at 40 °C for 24
323 hours. The extracts were then analyzed at ultra-high mass resolution using a Bruker Daltonik

324 Solarix 12T FT-ICR-MS. Ionization was carried out using an Apollo II ESI source and an APPI-II
325 source (all from Bruker Daltonik GmbH, Bremen, Germany).

326 For electrospray ionization (ESI⁻), nitrogen was used as the nebulizing gas at a flow rate of
327 4 L min⁻¹ at 220 °C and a pressure of 1.4 bar. The capillary voltage was set to 3000 V, and the
328 collision-induced dissociation (CID) voltage was 60 V. The samples were infused at a flow
329 rate of 2.5 µL min⁻¹ using a Hamilton syringe pump. The spectra were recorded in
330 broadband mode using 8-megaword data sets. The ion accumulation time was 0.05 s, and a
331 total of 200 scans were collected into the mass spectrum, covering a mass-to-charge ratio
332 (m/z) range of 150–1000. For atmospheric pressure photoionization (APPI⁺), nitrogen was
333 used as the nebulizing gas at a flow rate of 3 L min⁻¹ at 210 °C and a pressure of 12.3 bar.
334 The capillary voltage was set to - 1000 V, and the CID voltage was 30 V. The samples were
335 infused at a flow rate of 20 µL min⁻¹ using a Hamilton syringe pump. The spectra were
336 recorded in broadband mode using 8-megaword data sets. The ion accumulation time was
337 0.05 s, and a total of 300 scans were collected into the mass spectrum, covering an m/z
338 range of 147–1500.

339 The resulting spectra were internally recalibrated (quadratic) with a standard deviation
340 error of < 0.02 ppm, and only m/z values with a signal-to-noise ratio > 9 were exported for
341 formula assignment. Formula assignment was performed using a combination of Bruker
342 Analysis and Microsoft Excel, considering the isotopes ¹²C and ¹³C and the elemental ranges
343 C_xH_yN_{0–2}O_{0–10}S_{0–2}Na_{0–1}. The mass tolerance was set to 5 ppm.

344 **3. Results**

345 **3.1. Methane and carbon dioxide concentrations and cell abundances**

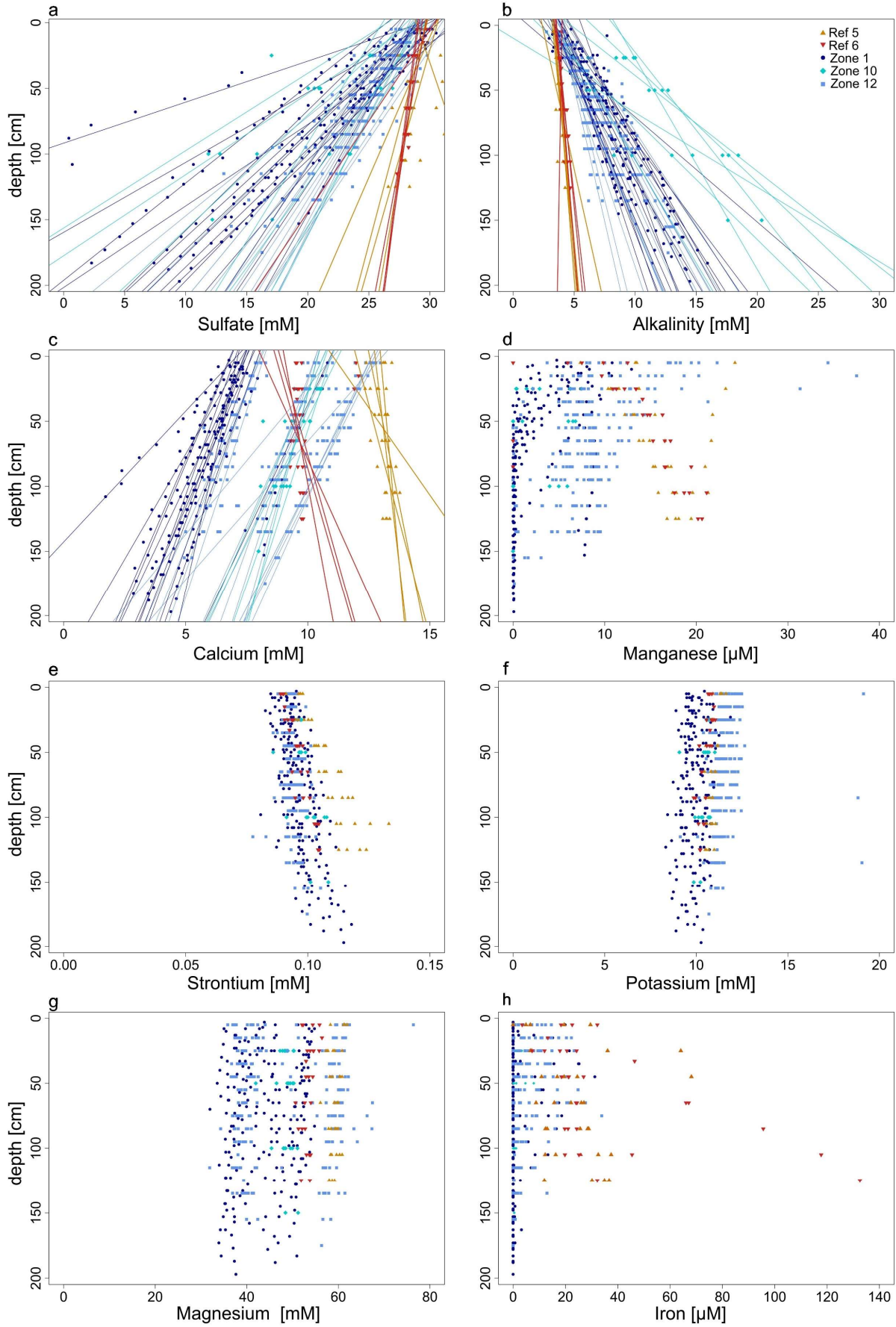
346 All samples contain measurable methane concentrations, ranging from 0.08 to 19.79 µM.
347 While samples from reference sites contain less than 5 µM of methane, higher
348 concentrations are restricted to few samples from HC-affected sites, all located deeper than
349 100 cm below seafloor (cmbsf). CO₂ was detectable in all samples, with concentrations
350 ranging from 29 µM to 512 µM, without any site-specific trend (Supplementary Fig. S1). This
351 is likely due to carbonate buffering, with dissolved CO₂ equilibrating with bicarbonate and

Imprint of minute hydrocarbon seepage on sedimentary fractions

352 carbonate in pore water at both HC-affected and reference sites. In both cases, low gas
353 concentrations prevented measurement of their stable isotopic signatures.

354 Total cell counts are approximately 10^7 cells \times cm³ across all sediment cores, with no
355 significant variation with depth (Supplementary Fig. S2). The mean deviation of cell counts
356 within samples is around 12%.

Imprint of minute hydrocarbon seepage on sedimentary fractions



357

358

Figure 2: Pore-water profiles for some representative parameters. The profiles for sulfate concentrations (a),

359 alkalinity (b), and calcium (c) show both data points and regression lines ($R^2 > 0.8$). The regression lines for HC-
 360 affected zones (Zone 1, Zone 10, Zone 12) show steeper gradients compared to those from reference zones
 361 (Ref 5, Ref 6). The profiles for magnesium (d), strontium (e), potassium (f), magnesium (g), and iron (h) are
 362 shown as data points due to the insufficient R^2 value of their respective regression lines.

363 **3.1. Pore water profiles**

364 Both sulfate and alkalinity concentrations exhibit strong linear decreasing and increasing
 365 trends ($R^2 \geq 0.85$) with depth (Figs. 2a and 2b), respectively. The gradients are steeper in the
 366 HC-affected zones compared to reference zones. Based on linear extrapolation, sulfate
 367 depletion would be reached at ca. 3 and 12 mbsf in HC and reference zones, respectively.
 368 Sulfide concentrations are below the detection limit ($1 \mu\text{M}$) in all cores from reference zones
 369 and in most of the cores from Z12 (only 2 out of 17 cores have detectable sulfide;
 370 Supplementary Fig. S3). In contrast, in most cores from Z01 (12 out of 15) and Z10 (4 out of
 371 7), sulfide concentrations increase with depth.

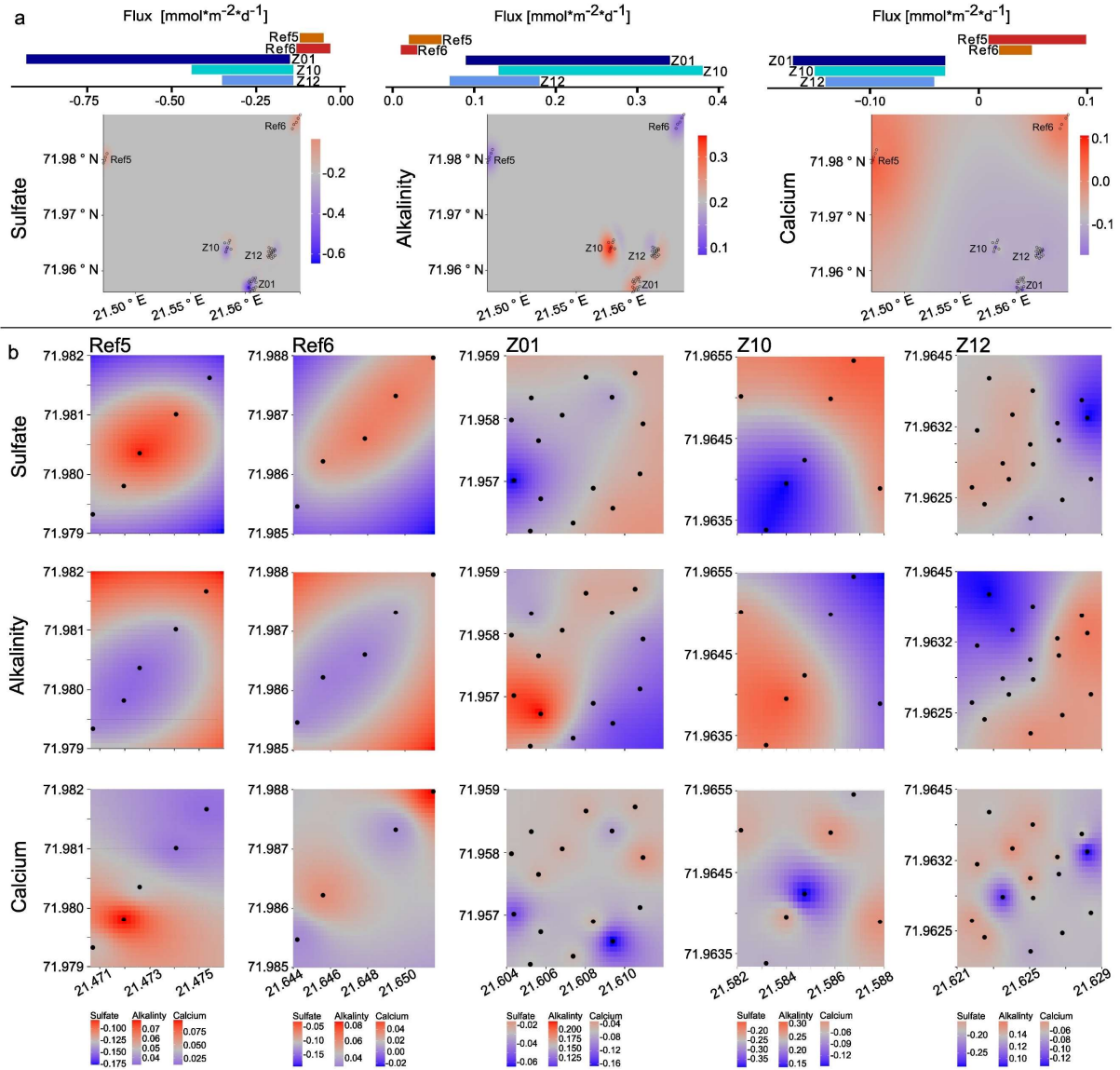
372 In the reference zones concentrations of pore water Ca^{2+} increase with depth (Fig. 2c,
 373 Supplementary Fig. S3), but decrease in the HC-affected zones. For Mn^{2+} concentrations also
 374 increase with depth in the reference zones (Fig. 2d, Supplementary Fig. S4). In most of the
 375 cores from HC-affected zones, Mn^{2+} pore water profiles show a decreasing trend with
 376 depth, but with distinct patterns, of which each one is predominant in a different sampling
 377 zone: (1) in Z01 many profiles show concentrations decreasing from ca. $15 \mu\text{M}$ at the SWI to
 378 near zero at ca. 75 cmbsf; (2) in Z12 concentrations decrease from ca. $15 \mu\text{M}$ at the SWI but
 379 then stabilize around $5 \mu\text{M}$ at 1 mbsf; (3) in Z10 and Z12 some concentrations profiles
 380 remain constant around 7 mM throughout depth.

381 Pore water concentrations for Cu^{2+} , Si^{4+} , Zn^{2+} , Mg^{2+} and K^+ remain almost unchanged in with
 382 depth in both HC-affected and reference zones (Figs. 2e-2g, Supplementary Figs. S4-S5),
 383 whereas Sr^{2+} concentrations increase in cores from both HC-affected zones and reference
 384 zones, but more pronounced for the latter (Fig. 2e). Dissolved Fe^{2+} is rarely detectable in
 385 cores from the HC-affected zones and falls below detection limit within the upper 1 mbsf
 386 (Fig. 2h). In most cores from reference zones, pore water Fe^{2+} is detectable and
 387 concentrations increase with depth. Ba^{2+} was measurable only in few cores from Z01, with

388 concentrations increasing with depth (Supplementary Fig S4). With few exceptions, Ni²⁺ and
 389 As²⁺ remain below the detection limit in all samples at all depths.

390 **3.2. Statistical analyses of inter- and intrazonal variations**

391 *3.2.1. Comparative analysis of pore water geochemistry*



392 **Figure 3. Spatial variability and flux patterns of sulfate, alkalinity, and calcium across different zones.** (a) Bar
 393 plots show the mean areal fluxes (mmol·m⁻²·d⁻¹) of sulfate (left), alkalinity (middle), and calcium (right) at the
 394 five zones (Ref5, Ref6, Z01, Z10, Z12). Kriging-interpolated maps illustrate the spatial distribution of these
 395 fluxes across the study area. Color gradients indicate the direction and magnitude of fluxes. (b) Detailed kriging
 396 maps of sulfate (top row), alkalinity (middle row), and calcium (bottom row) fluxes at each zone. Each column
 397 corresponds to one zone, showing localized spatial variability in solute fluxes. Black dots indicate the sampling
 398 sites.
 399

400 The Mann-Whitney U tests (Mann and Whitney, 1947) confirmed statistical significance for
401 steeper sulfate and alkalinity gradients (Fig. 2, Supplementary Table S2) in HC-affected
402 zones ($p_{\text{SO}_4} = 3.86\text{E-}10$, $p_{\text{alk}} = 2.74\text{E-}05$); opposite trends in Ca^{2+} profiles ($p_{\text{Ca}} = 1.40\text{E-}04$); and
403 different pore water gradients in Mn^{2+} concentrations ($p_{\text{Mn}} = 5.38\text{E-}06$), assuming linear
404 profiles which in some cases did not provide the best fit (Fig. 2, Supplementary Fig. S4 and
405 porewater profile descriptions in Section 3.1). The results for manganese should therefore
406 be considered as approximations.

407 The Brown-Forsythe tests (Brown and Forsythe, 1974) further confirmed that the variance
408 for pore water SO_4^{2-} , alkalinity, Ca^{2+} , and Mn^{2+} gradients is smaller within reference zones
409 (all p-values < 0.05, Supplementary Table S3) than within HC-affected zones (Fig. 2). In
410 addition, a comparison of the variances across individual HC zones and reference zones
411 indicates significant differences in most instances.

412 Kriging plots for sulfate, alkalinity and calcium fluxes (which are proportional to their
413 gradients) enabled the visualization of spatial variations over the entire study area and
414 within the sampling zones (Fig. 3). The resulting patterns of variability align with previous
415 statistical tests and highlight the different spatial heterogeneity between reference and HC-
416 affected areas, with notably a stronger variability among those exposed to seepage.

417 *3.2.2. Pore water species within and across cores*

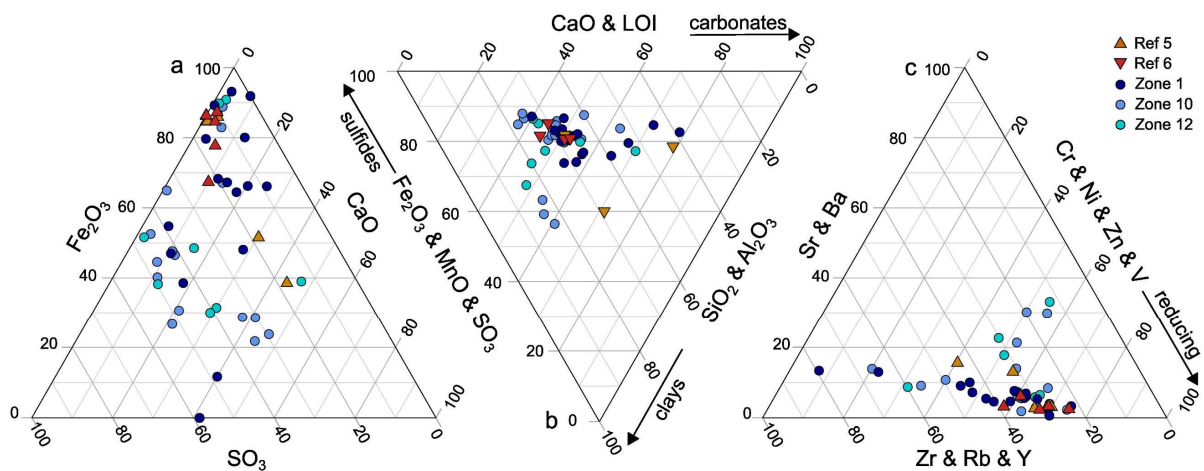
418 We also performed intra- and intervariation analyses, i.e. we investigated the correlation of
419 chemical species within each core using Pearson Correlation (Pearson, 1895; Sedgwick,
420 2012). We found a strong correlation (average $|r| > 0.86$) between sulfate, alkalinity and
421 calcium and, to a lesser extent (average $|r| > 0.66$) with manganese in almost every
422 individual core from HC zones. In contrast, within reference zones, we only found
423 correlations between alkalinity and sulfate (average $r > -0.76$) as well as alkalinity and
424 manganese (average $r > 0.86$) (Supplementary Table S4).

425 To determine whether concomitant biogeochemical processes may occur in different cores,
426 we assessed the correlation between pore water gradients for each of the 5 sampling zones
427 separately, resulting in 10 combinations of alkalinity, sulfate, manganese, calcium, and
428 sulfide. For cores from reference zones, a negative correlation between sulfate and

429 alkalinity was observed ($r = -0.80$ and -0.85 for Ref5 and Ref6). In addition, for Ref5,
 430 additional correlations were found between sulfate and manganese ($r = -0.99$), alkalinity
 431 and calcium ($r = -0.86$) and alkalinity and manganese ($r = 0.78$). For cores from the three HC
 432 HC zones, no significant correlations ($r < 0.7$) were found between geochemical species,
 433 except at Z10 between sulfate and alkalinity ($r = -0.89$), alkalinity and sulfide ($r = 0.77$)
 434 (Supplementary Table S4).

435 *3.2.3. XRF elemental concentrations of the sediment inorganic fraction*

436 CaO and SO_3 concentrations are significantly higher (Mann-Whitney U test, $p < 0.05$) in
 437 sediments from HC-affected than reference zones. Despite similar behavior as alkaline-earth
 438 elements, Ba ($p = 0.11$) and Sr ($p = 0.17$) were only slightly more abundant in sediments
 439 exposed to seepage. Conversely, the relative abundance of Fe_2O_3 , P_2O_5 , Ti, Cr, and Zn is
 440 higher ($p < 0.05$) in cores from reference zones, while Al ($p = 0.06$), Ni ($p = 0.05$), Mn ($p =$
 441 0.12), and V ($p = 0.05$) show a tendency towards higher relative abundances. The loss on
 442 ignition (LOI) is significantly higher ($p < 0.05$) in cores from reference zones.



443
 444 **Figure 4. Ternary diagrams showing the relative proportions of selected major and trace elements in solid**
 445 **phase sediments from hydrocarbon HC zones and reference zones.** (a) Major elements: Fe_2O_3 – SO_3 –CaO, (b)
 446 major elements grouped by associated mineral fractions: CaO and LOI (carbonate), Fe_2O_3 and MnO and SO_3
 447 (sulfide), and SiO_2 and Al_2O_3 (clay), and (c) trace elements grouped by geochemical behavior: Cr, Ni, Zn and V
 448 (redox-sensitive), Sr and Ba (calcite-, barite-associated), and Zr, Rb and Y (conservative). Each symbol
 449 represents an individual sample. HC zones (blue colors) and reference zones (red colors) largely overlap, the
 450 scatter in the HC zones is noticeably larger, indicating a greater variance.

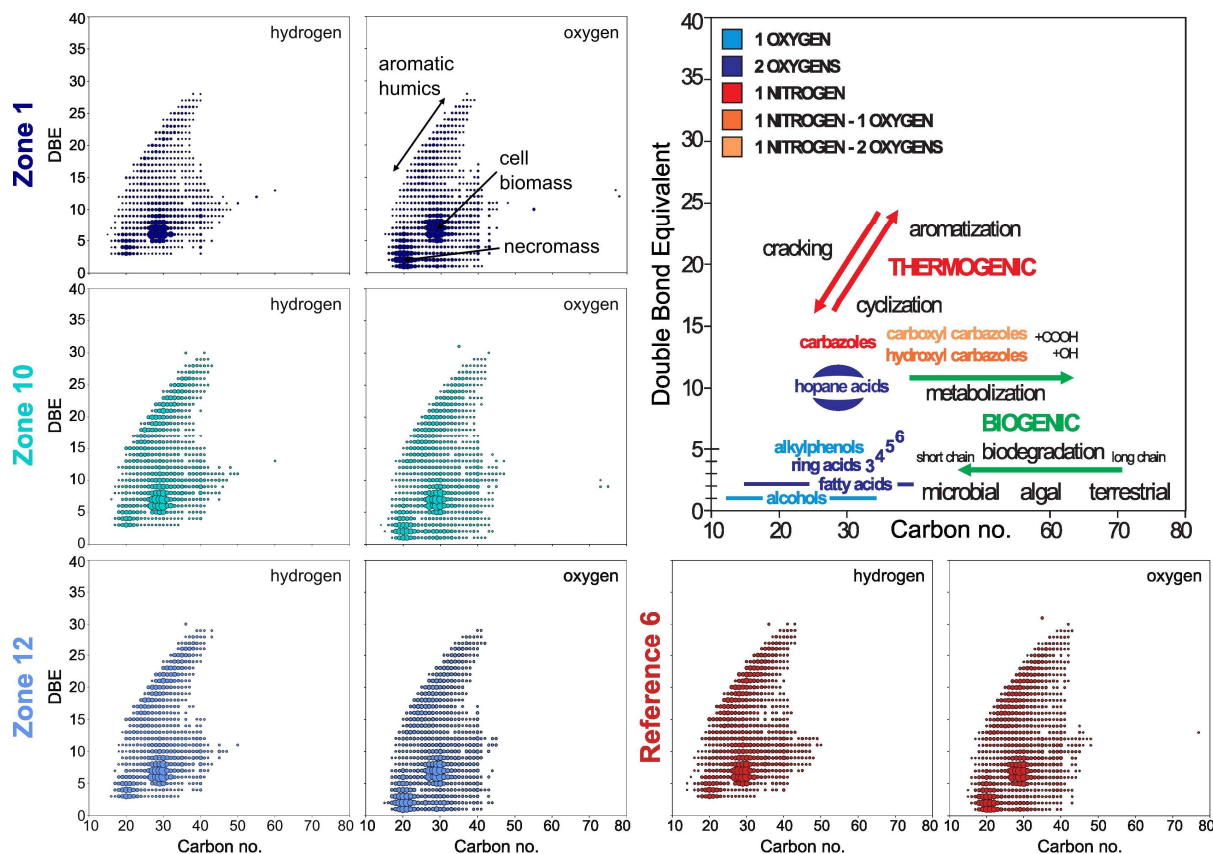
451 Significant differences ($p < 0.05$) revealed by the Brown-Forsythe variance homogeneity test
452 included Ba and SO_3 concentrations at seepage and reference zones, highlighting higher
453 variance among cores from HC-affected zones. Variance in CaO concentrations appeared
454 non-significant ($p = 0.09$). Major and trace element in ternary diagrams (Fig. 4) confirm this,
455 as the variance (scatter) is noticeably greater in the HC zones compared to the reference
456 zones. Despite considerable overlap, this observation is consistent with the results of the
457 Brown-Forsythe test, illustrating the lower variance across samples from reference zones
458 compared to HC zones. This pattern is further supported by PCA of major and trace
459 elements (Supplementary Figs. S6–S7), where samples from HC zones show greater
460 dispersion along the first principal component (60.7% and 59.8% variance explained,
461 respectively), indicating higher variability in both major and trace element composition.

462 **3.3. Organic compound classes across sampling zones**

463 The number of mass spectrometry signals and their distribution across different compound
464 classes (e.g., pure HCs, HCs with O, N, and S atoms), measured in both ionization modes
465 (APPI+ and ESI-) and analyzed in various data representations, appear very similar for both
466 seepage and reference sites. Atomic H/C and O/C ratios derived from assigned molecular
467 formulas showed no significant differences between seep and reference sites. Additionally,
468 the degree of unsaturation (i.e. double bond equivalent, DBE) relative to the number of
469 carbon atoms does not show significant variations in the relative abundance of different
470 compound classes or noticeable differences across sampling sites (Fig. 5, Supplementary Fig.
471 8).

472 Specific molecular signatures indicative of microbial biomass (e.g. hopanoids) and degraded
473 OM (e.g. humic acids) are also comparable across sampling zones (Fig. 5). Similar to total cell
474 counts, molecular clusters assigned to hopanoid-derived compounds (typically around 6–8
475 DBE and ~30 carbons) occur in similar abundance at all sites, suggesting comparable
476 microbial population sizes. Likewise, signals corresponding to fatty acids (low DBE, low
477 number of carbons), which can be interpreted as cell remnants or necromass, are evenly
478 distributed. Finally, aromatic compounds which are typically associated with humic
479 substances from highly degraded and refractory OM, are equally present in sediments from
480 all sampling zones. Signatures of seepage-related hydrocarbons, including saturated alkanes

481 and polyaromatic hydrocarbons typically associated with migrated oil and gas, were not
 482 detected.



483
 484 **Figure 5. Diagrams for molecular polar compounds identified by FT-ICR-MS in APPI+ mode in sediment**
 485 **extracts from the three hydrocarbon HC zones and one reference zone. (From left to right) Double bond**
 486 **equivalents (DBE) plotted against carbon number for compounds containing hydrogen and oxygen, and**
 487 **simplified interpretative framework of some molecular classes (e.g. aromatic acids, hopane acids,**
 488 **alkylphenols) and the expected shifts related to biogenic (e.g. microbial degradation) vs. thermogenic (e.g.**
 489 **cracking, aromatization) processes.**

490 **4. Discussion**

491 In the SW Barents Sea, sediments are particularly organic-lean, with TOC values below 0.5 %
 492 (Knies and Martinez, 2009). This low organic content enables the detection of discrete HC
 493 seeps, as even a slight supply of electron donors can result in a direct increase in the
 494 metabolic activity of HC-degrading microbial populations (Joye, 2020). This increase in
 495 metabolic activity, along with the resulting geochemical redox changes, can be distinguished
 496 from the background signal corresponding to pristine conditions at the seabed. In
 497 comparison, any microbial or geochemical signal arising from inconspicuous HC seepage in

498 organic-rich environments would be obscured by ongoing OM breakdown, hampering
499 discrimination of specific microbial populations or metabolic pathways involved in the
500 degradation of discrete HCs.

501 **4.1. Organic signatures of potentially active seepage remain elusive**

502 At seepage sites, we expected a greater diversity and higher concentrations of oxygen-
503 containing compounds in the FT-ICR-MS mass spectra due to the formation of aromatic-ring
504 radicals and by-products (e.g. alcohols, organic acids) during microbial HC degradation
505 (Radovic and Silva, 2025). In sediments not exposed to seepage, these compounds should
506 be less abundant, with overall a lower proportion of oxygenated components. However,
507 because seepage and reference sites showed similar compound class distributions (Fig. 5;
508 Supplementary Fig. S8), our data suggest that HCs had already been degraded at sediment
509 depths below the reach of our cores, or converted into compounds with chain lengths that
510 are too short for FT-ICR-MS detection. Instead, the FT-ICR-MS analysis only captured the
511 background signal of the subseafloor sediments (i.e. biomass, necromass, organic residues),
512 the corresponding compound class concentrations being consistent with similar microbial
513 cell counts across seepage and reference sites (Supplementary Fig. 2). Thus, the suitability of
514 this classical oil (and gas) analytical tool (Marshall and Rodgers, 2004) appears to be limited
515 in the context of inconspicuous seepage, indirectly supporting our basic assumption of
516 inconspicuous HC seepage in the HC-affected zones, without any indication for increased
517 microbial biomass at seep sites.

518 **4.2. Hydrocarbon seepage shapes redox zonation with precipitation of carbonate and** 519 **sulfide minerals**

520 Marine sediments exhibit a clear redox zonation, ranging from the aerobic respiration zone
521 near the surface, transiting through the nitrate, Mn^{4+} and Fe^{3+} reduction zones to the sulfate
522 reduction zone and methanogenesis (Froelich et al., 1979; Jørgensen and Kasten, 2006). In
523 the sulfate reduction zone, sulfate acts as the electron acceptor leading to the production of
524 hydrogen sulfide, bicarbonate, and water. The increase of these compounds in the pore
525 water promotes precipitation of carbonates (e.g. calcite) and sulfide minerals (e.g., pyrite)
526 (Smrzka et al., 2020; Smrzka et al., 2024; Lin et al., 2016; Peckmann et al., 2001).

527 Consequently, the incorporation of calcium, magnesium, strontium, iron, manganese, and
528 trace elements (e.g., Cu, Ni, Zn) into these minerals leads to their depletion in pore water
529 and enrichment in the sediment's inorganic fraction (Smrzka et al., 2019; Schippers and
530 Jørgensen, 2001).

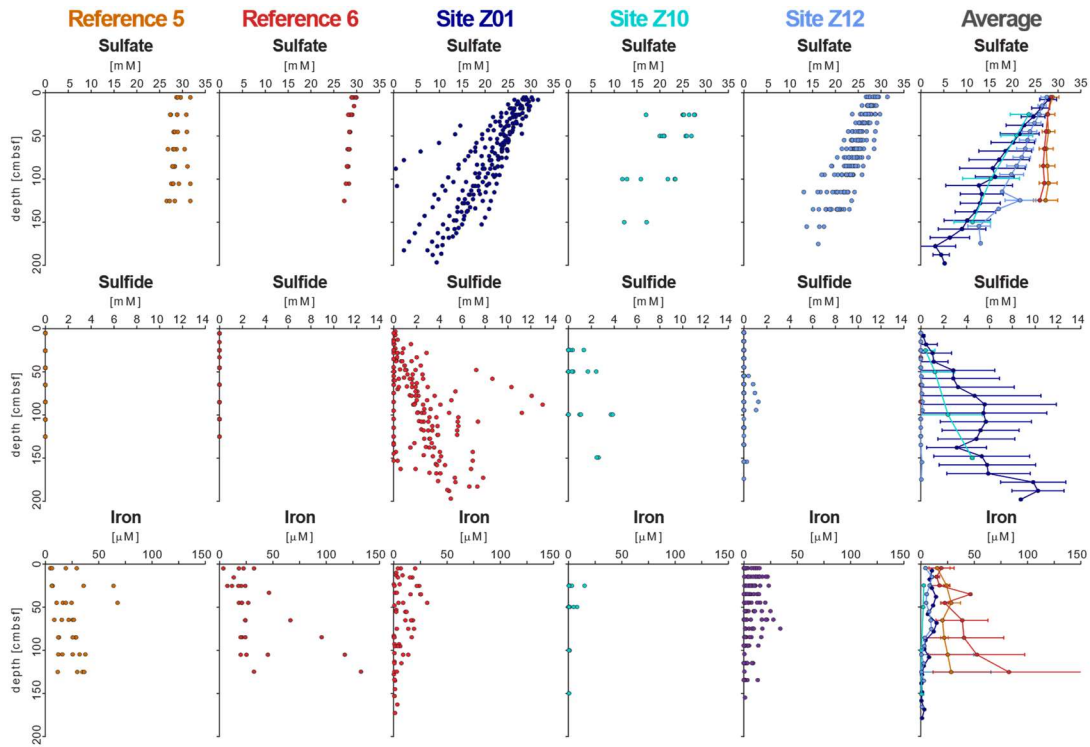
531 Both sediment geochemistry (Fig. 4, Supplementary Figs. S6-S7) and pore water analyses
532 (Fig. 2, Supplementary Figs. S3-S5) confirmed the presence of diagenetic carbonates in
533 sediments from HC zones. On the one hand, CaO, MgO, and Sr abundances increased in the
534 solid phase. On the other hand, pore water Ca²⁺ concentrations decreased while alkalinity
535 simultaneously increased with depth (Fig. 2). In contrast, Mg²⁺ and Sr²⁺ concentrations in
536 pore water remained largely unchanged. Notably, incorporation of Mg²⁺ and Sr²⁺ into
537 carbonate minerals is kinetically restricted compared to Ca²⁺ (Knight et al., 2023; Alkhatib et
538 al., 2022) and, as carbonate precipitation could occur over relatively short time periods (i.e.
539 during active seepage), substitution by pore water Mg²⁺ and Sr²⁺ appeared incomplete, thus
540 their concentrations remained almost unchanged. Although methane-derived carbonates
541 are typically high-Mg calcites or aragonite, we infer that the diagenetic carbonates in our
542 study are likely low-Mg calcites. Alternatively, the recrystallization of metastable carbonate
543 phases (e.g. aragonite) would release Sr²⁺ into the pore water (Hoareau et al., 2010). In
544 contrast to the HC zones, pore water alkalinity, Ca²⁺ and Sr²⁺ concentrations increase with
545 depth at the reference sites, while CaO and Sr contents remain low in the solid phase (Fig. 2,
546 Supplementary Fig. S3). These trends indicate that precipitation and dissolution of
547 carbonate minerals occurred (Schneider et al., 2006; Bach, 2024; Hoareau et al., 2010;
548 Smrzka et al., 2019) under seepage and non-seepage conditions, respectively.

549 Although barium (Ba²⁺) can theoretically substitute for Ca²⁺ in carbonate minerals, its larger
550 ionic radius and strong affinity for sulfate typically limit its incorporation. Instead, Ba²⁺
551 precipitates as barite (BaSO₄), which tends to dissolve under sulfate-reducing conditions
552 (Carter et al., 2020; Von Breyman et al., 1992). Indeed, Ba²⁺ was detectable in pore water
553 in only a few cores from HC-affected Zone 1 (Supplementary Fig. S4), where concentrations
554 increased with depth. This pattern suggests localized barite dissolution, likely triggered by
555 reducing conditions and upward fluid flow. Consistently, solid-phase data show elevated
556 Ba²⁺ concentrations in HC-affected zones relative to reference sites (Fig. 4, Supplementary

557 Tables S2), indicating barite accumulation through biogeochemical processes linked to HC
 558 seepage. These observations highlight the dynamic interplay between sulfate availability,
 559 redox zonation, and mineral precipitation at seepage sites, promoting barite formation but
 560 also sulfide mineralization.

561 At seepage sites, linear profiles in pore water sulfide revealed upward diffusion
 562 (Supplementary Fig. S3) and, given the low sulfate reduction rates previously measured in
 563 the corresponding interval (Schnabel et al., 2025), this sulfide likely originates from deeper
 564 sediment layers. When reactive metals, such as Fe^{2+} , Mn^{2+} , and other trace metals dissolved
 565 in pore water, meet with ascending sulfide, precipitation of metal sulfides occurs,
 566 contributing to an accumulation of redox sensitive metals and sulfur in the solid phase. This
 567 is in line with observations from e.g. seeps sites in Guaymas basin (Kars et al., 2025). At
 568 reference sites, dissolved sulfide is absent while Fe^{2+} and Mn^{2+} concentrations increase in
 569 the pore water (Fig. 6, Supplementary Fig. S3, Supplementary Fig. S4) , suggesting that
 570 anaerobic respiration of solid-phase Fe(III) and Mn(IV) oxides prevails over sulfate reduction
 571 and that precipitation of metal sulfides does not take place, at least not on a quantitatively
 572 significant level. Because higher pore water sulfide concentrations in our samples generally
 573 correlate with elevated sulfur (i.e. SO_3) (Fig. 6) concentrations in the solid phase, sulfide
 574 precipitation and sulfur accumulation allow to distinguish seepage sites from reference
 575 sites, where they remain systematically low. This further demonstrates that local differences
 576 in sulfide production or flux rates, as well as metal availability, may result from seepage in
 577 the sediment.

Imprint of minute hydrocarbon seepage on sedimentary fractions



578

579 **Figure 6. Porewater profiles of sulfate, sulfide, and dissolved iron across five sites, including site**
 580 **averages. In seep-affected cores, iron concentrations decrease where sulfide increases, indicating**
 581 **removal of reactive iron through sulfide precipitation. Sulfate generally decreases with depth across**
 582 **all sites. Error bars represent site-specific averages where applicable.**

583 Besides major element dynamics, HC seepage also alters biogeochemical cycling of trace
 584 metals through its influence on redox zonation and authigenic mineral formation, thereby
 585 exerting control on their mobility or retention in the sediment column. Trace element
 586 incorporation into sulfide minerals vary between oil- and methane-dominated seep
 587 environments, with higher concentrations of elements like Mn, Mo, Cu, and Zn often
 588 observed in oil seep pyrites (Smrzka et al., 2024). At both seepage and reference zones,
 589 redox-sensitive trace metals (e.g. Zn, Ni, and V; Cr to a lesser extent) can be transported in
 590 solution upward from deeper sediment layers and precipitate locally depending on sulfate
 591 reduction and other redox-dependent activities. At seepage sites, methanotrophic sulfate
 592 reduction and AOM-driven processes enhance neoformation of sulfides and carbonates
 593 which act as sinks for trace metals at seep sites, in particular pyrite (Smrzka et al. (2019);
 594 Smrzka et al. (2024); Miao et al. (2022)). In contrast, lower SR activity and lesser mineral
 595 precipitation at reference sites allow trace elements to continuously diffuse upward and be
 596 captured under suboxic conditions via adsorption or precipitation as iron (oxyhydr)oxides.
 597 Altogether, despite similar concentrations in the pore fluid across sampling sites

598 (Supplementary Table S2), the degree and depth of occurrence of sulfate reduction govern
599 whether dissolved metal ions are sequestered in specific geochemical zones or bypass the
600 redox gradient. Nevertheless, trace metal concentrations may also vary with redox
601 gradients, precipitation kinetics, and phase-specific affinities (Smrzka et al. (2019),
602 hampering the use of pore water or solid phase concentration as a proxy for HC seepage.
603 Hence, a combined assessment of pore water geochemistry, redox zonation, and authigenic
604 minerals offers a more suitable approach for seepage characterization. Although our bulk
605 sediment geochemical data do not specifically target sulfide mineral phases, these findings
606 highlight the potential of geochemical signatures to record different seepage types.

607 4.3. Pore water fluxes and diagenetic minerals reflect the dynamics of transient seepage

608 Linear profiles for pore water alkalinity, SO_4^{2-} , and Ca^{2+} suggest no net turnover within the
609 sampled sediment interval (Schulz, 2006). This stands in contradiction with our observations
610 of the solid-phase geochemistry, which is indicative of carbonate and sulfide mineral
611 formation in HC-affected zones. We suggest that the sulfate-methane transition zone
612 (SMTZ), where most sulfide and carbonate precipitation occur, may have undergone
613 temporal and spatial depth fluctuations, driven by variations in HC flux over time. Such
614 fluctuations are well-documented and influenced by multiple factors, including
615 sedimentation rate, temperature, OM availability (Dale et al., 2008) and hydrostatic
616 pressure, which in the Barents Sea is particularly shaped by glacial-interglacial dynamics
617 (Argentino et al., 2021; Nickel, 2013).

618 In the Barents Sea, low sedimentation rates combined with extensive glacial history are
619 inferred to have shaped SMTZ dynamics. During the Last Glacial Maximum (~20 ka),
620 grounded ice sheets prevented seawater sulfate diffusion into the sediment in the Barents
621 Sea (Andreassen et al., 2008; Siegert et al., 2001), shifting the SMTZ upward. Following
622 deglaciation (~14 ka) (Elverhøi et al., 1993), seawater reoccupied the seafloor, restoring
623 sulfate supply and initiating a progressive downward migration of the SMTZ. Processes such
624 as gas hydrate dissociation and associated methane release during ice retreat (Nickel et al.,
625 2013) further enhanced these dynamics. Comparable patterns have been observed
626 elsewhere in the Barents Sea, where post-glacial rebound and HC flux variations have
627 caused significant SMTZ fluctuations (Argentino et al., 2021).

628 The occurrence of diagenetic carbonates and sulfides resulting most probably from past
629 AOM processes at the (paleo)SMTZ are therefore best understood as products of these
630 historical boundary conditions. Their accumulation in the sediment, in combination with
631 present-day linear pore water profiles, suggests that the system currently reflects a stage of
632 subdued seepage activity, and consequently deeper SMTZ. Thus, the present-day mineral
633 assemblage provides a cumulative archive of past seepage episodes rather than a snapshot
634 of ongoing processes, highlighting a key limitation of interpreting solid-phase geochemistry
635 alone. Although an increased presence of carbonates and sulfides may be indicative of past
636 redox conditions and fluid flow, these minerals cannot reliably distinguish active from relict
637 seepage. Integration with pore water profiles and other dynamic indicators remains
638 essential to reconstruct seepage history and assess present-day activity.

639 Overall, our findings align with typical mineralogical signatures of weak HC seeps, commonly
640 with carbonate (CaO) contents of 1-3 wt% (Rovere et al., 2020; Karaca et al., 2010) and
641 sulfur (SO₃) concentrations below 1 wt % (Fischer et al., 2012), thereby matching our
642 seepage site values (i.e. 2.1 wt% CaO, 0.8 wt% SO₃). The reference sites or our study exhibit
643 values (i.e. 1.5 wt% CaO, 0.2 wt% SO₃) that are consistent with background diagenesis
644 typically observed in non-seep environments (1–2 wt% CaO, <0.2 wt% SO₃) (Fischer et al.,
645 2012; Karaca et al., 2010). Thus, we observe that carbonate and sulfide enrichments
646 documented in Barents Sea sediments represent the imprint of past seepage episodes,
647 whereas present-day pore water profiles reflect a current state of low, or absent, HC flux
648 within the sampled interval.

649 **4.4. Fine-scale heterogeneity characterizes weak hydrocarbon seepage**

650 The HC zones are affected by inconspicuous, diffuse seepage with very low sulfate flux rates
651 below 1 mmol × m⁻² × d⁻¹ (Fig. 3). Typical fluxes at seeps range from 1–10 mol × m⁻² × d⁻¹ for
652 high flux seeps, e.g. Coal Oil Point Seep Field, Santa Barbara, California (Padilla et al., 2019),
653 and 0.1–1 mol × m⁻² × d⁻¹ for moderate flux seeps, e.g. North-western Black Sea (Hu et al.,
654 2012). Since seepage-induced biogeochemical processes, like AOM and concomitant
655 carbonate precipitation, predominantly occur below our sampling depth range (Schnabel et
656 al., 2025), their effects can be detected only indirectly. For instance, the steeper sulfate
657 gradients observed in the HC zones compared to the reference zones (Fig. 3, Supplementary

658 Fig. S3) suggest increased sulfate reduction rates due to HC supply from below. Geochemical
659 fluxes at the seepage sites show considerable variability across individual cores (Fig. 3),
660 which is considered a typical feature of seep environments inherent to localized differences
661 in fluid flow, microbial activity, or redox conditions (Pop Ristova et al., 2015; Foster et al.,
662 2015; Schnabel et al., 2025). In contrast, reference sites present rather uniform conditions,
663 as they primarily reflect sedimentation, OM input and diffusion at the sediment-water
664 interface rather than seepage.

665 In addition to variable fluxes reported for cores from seepage sites, the pattern of
666 interconnected geochemical parameters also differs on a spatial scale (Supplementary Table
667 S4). While a single pore water species may correlate in all 50 individual cores (e.g. sulfate
668 concentrations and alkalinity), ratios between parameters appear to be different for each
669 core across different HC-affected sites, and even within each individual seepage site
670 sampled. This suggests that, even though similar microbial processes (e.g. denitrification
671 reduction, sulfate reduction), can be expected to take place throughout the sampled area,
672 their degree of intensity and interactions vary on a small spatial scale, leading to
673 considerable local differences both within and between HC zones. In contrast, such
674 correlations are much better both within and across cores from reference sites (Fig. 5),
675 indicating more homogeneous and predictable diagenetic conditions.

676 **5. Conclusions**

677 This study elucidates the geochemical and mineralogical imprints of inconspicuous HC
678 seepage on near-seafloor sediments in the southwestern Barents Sea. Extremely low
679 element fluxes with often complete degradation of HCs in sediment layers below the
680 sampling depth of this study posed significant challenges in the detection of active seepage.
681 This explains why the FT-ICR-MS-based approach was unsuccessful in identifying diagnostic
682 organic compounds, as volatile and short-chained organic compounds cannot be resolved.
683 In contrast, inorganic geochemical signatures provided indirect evidence of seepage-related
684 reductive diagenetic processes. Elevated pore water alkalinity alongside decreasing Ca^{2+}
685 concentrations with depth, substantiated by elemental enrichments in the solid phase were
686 clear indications of carbonate precipitation. In addition, pore water depletion of sulfate and

687 manganese concomitant with increased solid phase sulfide concentrations point towards
688 formation of sulfide minerals. In summary, many geochemical processes along strong seeps
689 can also be directly or indirectly detected for minor HC seeps where the HCs are
690 metabolized below the sampling interval.

691 Pronounced spatial variability in geochemical gradients across seepage-affected sites was
692 observed, revealing local heterogeneity in fluid flow and redox conditions as a result of
693 variable seepage intensity. Otherwise, correlated geochemical parameters within single
694 cores pointed to consistent coupling with past and present biogeochemical processes.
695 Altogether, these spatial patterns underline the relevance of a targeted sampling strategy to
696 resolve geochemical heterogeneities in the shallow subseafloor, which proves essential for
697 capturing the transient nature of seepage. Fine-scale geochemical variations are easily
698 overlooked but are nonetheless crucial for understanding seep dynamics and differentiating
699 between active and past seepage processes, requiring adequate spatial and temporal
700 coverage and geostatistical techniques.

701 **6. Data availability**

702 The geochemical data is available on PANGAEA as dataset #974341 and #974346 under
703 digital object identifier <https://doi.pangaea.de/10.1594/PANGAEA.974341> and
704 <https://doi.pangaea.de/10.1594/PANGAEA.974346>.

705 **7. Author contributions**

706 JK and RDP organized the sampling cruise. ES and JK designed the study and collected
707 samples. ES performed cell counts and analyzed pore water geochemistry under the
708 supervision of JK. XRF measurements were performed under the supervision of JS. FT-ICR-
709 MS analyses of organic extracts were carried out by KM and SP. ES analyzed the data in
710 collaboration with AV, JK and SP. ES wrote the manuscript with input and revisions from all
711 co-authors.

712 **8. Competing interests**

713 The authors declare that they have no conflict of interest.

714 **9. Acknowledgements**

715 We thank all crew members of the RV *Sverdrup II*, Steffen Okolski, J. Axel Kitte and Edgar
716 Kutschera for their great help during the sampling cruise. The help of Steffen Okolski in pore
717 water analyses is acknowledged. We acknowledge the support of Anja Schleicher, Andrea
718 Gottsche and Heike Rothe in performing the XRF and ICP-MS measurements, including
719 sample melting and instrument operation. Sabine Kasten and Bo Liu are thanked for advices
720 on data processing.

721 **10. Financial support**

722 This research has received funding from the European Union's Horizon 2020 research and
723 innovation programme under grant agreement no. 899667. The article processing charge for
724 this open-access publication were covered by GFZ Helmholtz Centre for Geosciences.

725

726 The PROSPECTOMICS Consortium

727 The principal investigators of the PROSPECTOMICS project are Jens Kallmeyer¹, Paul
728 Wilmes², Alexander J. Probst³, Dörte Becher⁴, Thomas Rattai⁵, and Rolando di Primio⁶. The
729 project managers are Aurèle Vuillemin¹, Cédric L. Laczny², André R. Soares³, and Anke
730 Trautwein-Schult⁴. Scientists and technicians include Ellen Schnabel¹, Kai Mangelsdorf⁷,
731 Steffen Okolski¹, J. Axel Kitte¹, Benoit Kunath², Zainab Zafar², Sarah Esser³, Anne Ostrzinski⁴,
732 Sebastian Grund⁴, and Alexander Pfundner⁵.

733 ¹GFZ Helmholtz Centre for Geosciences, Section Geomicrobiology, Telegrafenberg, 14473
734 Potsdam, Germany; ²Luxembourg Centre for Systems Biomedicine, University of
735 Luxembourg, Esch-sur-Alzette; ³Environmental Metagenomics, Research Center One Health
736 Ruhr of the University Alliance Ruhr, Faculty of Chemistry, University of Duisburg-Essen,
737 Essen, Germany; ⁴Department of Microbial Proteomics, University of Greifswald, Greifswald,
738 Germany; ⁵Computational Systems Biology, Centre for Microbiology and Environmental
739 Systems Science, University of Vienna, Vienna, Austria; ⁶Aker BP ASA, Sandvika, Viken,

740 Norway; ⁷GFZ Helmholtz Centre for Geosciences, Section, Section Organic Geochemistry,
741 Telegrafenberg, 14473 Potsdam, Germany.

742 **11. References**

743 Abrams, M. A.: Significance of hydrocarbon seepage relative to petroleum generation and
744 entrapment, *Marine and Petroleum Geology*, 22, 457-477,
745 <https://doi.org/10.1016/j.marpetgeo.2004.08.003>, 2005.

746 Abrams, M. A.: Marine seepage variability and its impact on evaluating the surface migrated
747 hydrocarbon seep signal, *Marine and Petroleum Geology*, 121, 13,
748 <https://doi.org/10.1016/j.marpetgeo.2020.104600>, 2020.

749 Alkhatib, M., Qutob, M., Alkhatib, S., and Eisenhauer, A.: Influence of precipitation rate and
750 temperature on the partitioning of magnesium and strontium in calcite overgrowths,
751 *Chemical Geology*, 599, <https://doi.org/10.1016/j.chemgeo.2022.120841>, 2022.

752 Andreassen, K., Laberg, J. S., and Vorren, T. O.: Seafloor geomorphology of the SW Barents
753 Sea and its glaci-dynamic implications, *Geomorphology*, 97, 157-177,
754 <https://doi.org/10.1016/j.geomorph.2007.02.050>, 2008.

755 Argentino, C., Waghorn, K. A., Vadakkepuliambatta, S., Polteau, S., Bunz, S., and Panieri, G.:
756 Dynamic and history of methane seepage in the SW Barents Sea: new insights from
757 Leirdjupet Fault Complex, *Sci Rep*, 11, 4373, <https://doi.org/10.1038/s41598-021-83542-0>,
758 2021.

759 Bach, L. T.: The additionality problem of ocean alkalinity enhancement, *Biogeosciences*, 21,
760 261-277, <https://doi.org/10.5194/bg-21-261-2024>, 2024.

761 Berner, R. A.: A new geochemical classification of sedimentary environments, *Journal of*
762 *Sedimentary Research*, 51, 359-365, [https://doi.org/10.1306/212f7c7f-2b24-11d7-](https://doi.org/10.1306/212f7c7f-2b24-11d7-8648000102c1865d)
763 [8648000102c1865d](https://doi.org/10.1306/212f7c7f-2b24-11d7-8648000102c1865d), 1981.

764 Bowles, M. W., Mogollon, J. M., Kasten, S., Zabel, M., and Hinrichs, K. U.: Global rates of
765 marine sulfate reduction and implications for sub-sea-floor metabolic activities, *Science*,
766 344, 889-891, <https://doi.org/10.1126/science.1249213>, 2014.

767 Bradley, J. A., Arndt, S., Amend, J. P., Burwicz, E., Dale, A. W., Egger, M., and LaRowe, D. E.:
768 Widespread energy limitation to life in global subseafloor sediments, *Sci Adv*, 6, eaba0697,
769 <https://doi.org/10.1126/sciadv.aba0697>, 2020.

770 Brown, M. B. and Forsythe, A. B.: Robust Tests for the Equality of Variances, *Journal of the*
771 *American Statistical Association*, 69, 364-367,
772 <https://doi.org/10.1080/01621459.1974.10482955>, 1974.

- 773 Carter, S. C., Paytan, A., and Griffith, E. M.: Toward an Improved Understanding of the
 774 Marine Barium Cycle and the Application of Marine Barite as a Paleoproductivity Proxy,
 775 *Minerals*, 10, <https://doi.org/10.3390/min10050421>, 2020.
- 776 Chavez, F. P., Messié, M., and Pennington, J. T.: Marine primary production in relation to
 777 climate variability and change, *Annual Review of Marine Science*, 3, 227–260,
 778 <https://doi.org/10.1146/annurev.marine.010908.163917>, 2011.
- 779 Ciotoli, G., Procesi, M., Etiope, G., Fracassi, U., and Ventura, G.: Influence of tectonics on
 780 global scale distribution of geological methane emissions, *Nat Commun*, 11, 2305,
 781 <https://doi.org/10.1038/s41467-020-16229-1>, 2020.
- 782 Cline, J. D.: Spectrophotometric Determination of Hydrogen Sulfide in Natural Waters¹,
 783 *Limnol Oceanogr*, 14, 454-458, <https://doi.org/10.4319/lo.1969.14.3.0454>, 1969.
- 784 Dale, A. W., Aguilera, D. R., Regnier, P., Fossing, H., Knab, N. J., and Jorgensen, B. B.:
 785 Seasonal dynamics of the depth and rate of anaerobic oxidation of methane in Aarhus Bay
 786 (Denmark) sediments, *Journal of Marine Research*, 66, 127-155,
 787 <https://doi.org/10.1357/002224008784815775>, 2008.
- 788 de Groot, T. R., Kalenitchenko, D., Moser, M., Argentino, C., Panieri, G., Lindgren, M.,
 789 Dølven, K. O., Ferré, B., Svenning, M. M., and Niemann, H.: Methanotroph activity and
 790 connectivity between two seep systems north off Svalbard, *Frontiers in Earth Science*, 12,
 791 <https://doi.org/10.3389/feart.2024.1287226>, 2024.
- 792 Dong, H., Jaisi, D. P., Kim, J., and Zhang, G.: Microbe-clay mineral interactions, *American*
 793 *Mineralogist*, 94, 1505-1519, <https://doi.org/10.2138/am.2009.3246>, 2009.
- 794 Doré, A. G.: Barents Sea Geology, Petroleum Resources and Commercial Potential, *ARCTIC*,
 795 48, 207-221, 1995.
- 796 Edenborn, H. M., Paquin, Y., and Chateauneuf, G.: Bacterial contribution to manganese
 797 oxidation in a deep coastal sediment, *Estuarine, Coastal and Shelf Science*, 21, 801-815,
 798 [https://doi.org/10.1016/0272-7714\(85\)90074-5](https://doi.org/10.1016/0272-7714(85)90074-5), 1985.
- 799 Eichhubl, P., Davatzes, N. C., and Becker, S. P.: Structural and diagenetic control of fluid
 800 migration and cementation along the Moab fault, Utah, *Aapg Bulletin*, 93, 653-681,
 801 <https://doi.org/10.1306/02180908080>, 2009.
- 802 Elverhøi, A. and Solheim, A.: The Barents Sea ice sheet - a sedimentological discussion, *Polar*
 803 *Research*, 1, 23-42, <https://doi.org/10.1111/j.1751-8369.1983.tb00729.x>, 1983.
- 804 Elverhøi, A., Fjeldskaar, W., Solheim, A., Nyland-Berg, M., and Russwurm, L.: The Barents Sea
 805 Ice Sheet - a model of its growth and decay during the last ice maximum, *Quaternary*
 806 *Science Reviews*, 12, 11, [https://doi.org/10.1016/0277-3791\(93\)90025-H](https://doi.org/10.1016/0277-3791(93)90025-H), 1993.
- 807 Etiope, G.: *Natural Gas Seepage- The Earth's Hydrocarbon Degassing*, Springer, ISBN 978-3-
 808 319-14601-0, 2015.

- 809 Faleide, J. I., Gudlaugsson, S. T., and Jacquart, G.: Evolution of the western Barents Sea,
 810 Marine and Petroleum Geology, 1, 123-150, [https://doi.org/10.1016/0264-8172\(84\)90082-](https://doi.org/10.1016/0264-8172(84)90082-5)
 811 5, 1984.
- 812 Fischer, D., Sahling, H., Nöthen, K., Bohrmann, G., Zabel, M., and Kasten, S.: Interaction
 813 between hydrocarbon seepage, chemosynthetic communities, and bottom water redox at
 814 cold seeps of the Makran accretionary prism: insights from habitat-specific pore water
 815 sampling and modeling, Biogeosciences, 9, 2013-2031, [https://doi.org/10.5194/bg-9-2013-](https://doi.org/10.5194/bg-9-2013-2012)
 816 2012, 2012.
- 817 Foster, K. L., Stern, G. A., Carrie, J., Bailey, J. N., Outridge, P. M., Sanei, H., and Macdonald, R.
 818 W.: Spatial, temporal, and source variations of hydrocarbons in marine sediments from
 819 Baffin Bay, Eastern Canadian Arctic, Sci Total Environ, 506-507, 430-443,
 820 <https://doi.org/10.1016/j.scitotenv.2014.11.002>, 2015.
- 821 Froelich, P. N., Klinkhammer, G. P., Bender, M. L., Luedtke, N. A., Heath, G. R., Cullen, D.,
 822 Dauphin, P., Hammond, D., Hartman, B., and Maynard, V.: Early oxidation of organic matter
 823 in pelagic sediments of the eastern equatorial Atlantic: suboxic diagenesis, Geochimica et
 824 Cosmochimica Acta, 43, 1975-1090, [https://doi.org/10.16/0016-7037\(79\)90095-4](https://doi.org/10.16/0016-7037(79)90095-4), 1979.
- 825 Gabrielsen, R. H., Faerseth, R. B., Jensen, L. N., Kalheim, J. E., and Riis, F.: Structural elements
 826 of the Norwegian continental shelf, Part 1: The Barents Sea Region, NPD Bulletin, 6, 1-33,
 827 1990.
- 828 Heggland, R.: Gas seepage as an indicator of deeper prospective reservoirs. A study based
 829 on exploration 3D seismic data, Marine and Petroleum Geology, 15, 1-9,
 830 [https://doi.org/10.1016/S0264-8172\(97\)00060-3](https://doi.org/10.1016/S0264-8172(97)00060-3), 1998.
- 831 Hinrichs, K. U., Hayes, J. M., Sylva, S. P., Brewer, P. G., and DeLong, E. F.: Methane-
 832 consuming archaeobacteria in marine sediments, Nature, 398, 802-805,
 833 <https://doi.org/10.1038/19751>, 1999.
- 834 Hoareau, G., Monnin, C., and Odonne, F.: A study of celestine equilibrium in marine
 835 sediments using the entire ODP/IODP porewater data base, Geochimica et Cosmochimica
 836 Acta, 74, 3925-3937, <https://doi.org/10.1016/j.gca.2010.03.033>, 2010.
- 837 Hu, L., Yvon-Lewis, S. A., Kessler, J. D., and MacDonald, I. R.: Methane fluxes to the
 838 atmosphere from deepwater hydrocarbon seeps in the northern Gulf of Mexico, Journal of
 839 Geophysical Research: Oceans, 117, <https://doi.org/10.1029/2011jc007208>, 2012.
- 840 Hu, T., Luo, M., Qi, Y., He, D., Chen, L., Xu, Y., and Chen, D.: Molecular evidence for the
 841 production of labile, sulfur-bearing dissolved organic matter in the seep sediments of the
 842 South China Sea, Water Res, 233, 119732, <https://doi.org/10.1016/j.watres.2023.119732>,
 843 2023.
- 844 Huerta-Diaz, M. A. and Morse, J. W.: Pyritization of trace metals in anoxic marine sediments,
 845 Geochimica et Cosmochimica Acta, 56, 2681-2702, [https://doi.org/10.1016/0016-](https://doi.org/10.1016/0016-7037(92)90353-k)
 846 7037(92)90353-k, 1992.

- 847 Hunt, J. M.: *Petroleum Geochemistry and Geology*, W.H.Freeman & Co Ltd, New York, ISBN
848 9780716724414, 1995.
- 849 Hvoslef, S., Christie, O. H. J., Sassen, R., Kennicutt, M. C., Requejo, A. G., and Brooks, J. M.:
850 Test of a new surface geochemistry tool for resource prediction in frontier areas, *Marine*
851 *and Petroleum Geology*, 13, 107-124, [https://doi.org/10.1016/0264-8172\(95\)00032-1](https://doi.org/10.1016/0264-8172(95)00032-1), 1996.
- 852 Iversen, N. and Jørgensen, B. B.: Diffusion coefficients of sulfate and methane in marine
853 sediments: Influence of porosity, *Geochemica et Cosmochemica Acta*, 57, 571-778,
854 [https://doi.org/10.1016/0016-7037\(93\)90368-7](https://doi.org/10.1016/0016-7037(93)90368-7), 1993.
- 855 Johansen, S. E., Ostisty, B. K., Birkeland, Ø., Fedorovsky, Y. F., Martirosjan, V. N., Bruun
856 Christensen, O., Cheredeev, S. I., Ignatenko, E. A., and Margulis, L. S.: Hydrocarbon potential
857 in the Barents Sea region: play distribution and potential, *Norwegian Petroleum Society*
858 *Special Publications*, 2, 273-320, <https://doi.org/10.1016/B978-0-444-88943-0.50024-1>,
859 1993.
- 860 Jørgensen, B. B.: Mineralization of organic matter in the sea bed—the role of sulphate
861 reduction, *Nature*, 296, 643-645, <https://doi.org/10.1038/296643a0>, 1982.
- 862 Jørgensen, B. B. and Kasten, S.: Sulfur Cycling and Methane Oxidation, in: *Marine*
863 *Geochemistry*, 271-309, https://doi.org/10.1007/3-540-32144-6_8, 2006.
- 864 Jørgensen, B. B., Findlay, A. J., and Pellerin, A.: The Biogeochemical Sulfur Cycle of Marine
865 Sediments, *Front Microbiol*, 10, 849, <https://doi.org/10.3389/fmicb.2019.00849>, 2019.
- 866 Joye, S. B.: The Geology and Biogeochemistry of Hydrocarbon Seeps, *Annual Review of Earth*
867 *and Planetary Sciences*, 48, 205-231, [https://doi.org/10.1146/annurev-earth-063016-](https://doi.org/10.1146/annurev-earth-063016-020052)
868 [020052](https://doi.org/10.1146/annurev-earth-063016-020052), 2020.
- 869 Joye, S. B., Bowles, M. W., and Ziervogel, K.: Marine Biogeochemical Cycles, in: *The Marine*
870 *Microbiome*, 623-671, https://doi.org/10.1007/978-3-030-90383-1_15, 2022.
- 871 Joye, S. B., Boetius, A., Orcutt, B. N., Montoya, J. P., Schulz, H. N., Erickson, M. J., and Lugo,
872 S. K.: The anaerobic oxidation of methane and sulfate reduction in sediments from Gulf of
873 Mexico cold seeps, *Chemical Geology*, 205, 219-238,
874 <https://doi.org/10.1016/j.chemgeo.2003.12.019>, 2004.
- 875 Judd, A. and Hovland, M.: *Seabed fluid flow- The impact on geology, biology and the marine*
876 *environment*, Cambridge University Press, <https://doi.org/10.1017/cbo9780511535918>,
877 2009.
- 878 Kallmeyer, J., Smith, D. C., Spivack, A. J., and D'Hondt, S.: New cell extraction procedure
879 applied to deep subsurface sediments, *Limnology and Oceanography: Methods*, 6, 236-245,
880 <https://doi.org/10.4319/lom.2008.6.236>, 2008.
- 881 Karaca, D., Hensen, C., and Wallmann, K.: Controls on authigenic carbonate precipitation at
882 cold seeps along the convergent margin off Costa Rica, *Geochemistry, Geophysics,*
883 *Geosystems*, 11, <https://doi.org/10.1029/2010gc003062>, 2010.

- 884 Kars, M. A. C., Pastor, L., Burin, C., and Koornneef, L. M. T.: Data report: characterization of
 885 iron oxides and iron sulfides in sediments from IODP Expedition 385 Sites U1549 and U1552
 886 using rock magnetism and geochemistry, in: Proceedings of the International Ocean
 887 Discovery Program, Teske, A., Lizarralde, D., Höfig, T. W., and the Expedition 385 Scientists
 888 (Eds.), Volume 385, 19 pp., International Ocean Discovery Program,
 889 <https://doi.org/10.14379/iodp.proc.385.207.2025>, 2025.
- 890 Kasten, S. and Jørgensen, B. B.: Sulfate Reduction in Marine Sediments, in: Marine
 891 Geochemistry, Springer, Heidelberg, 263-281, [https://doi.org/10.1007/978-3-662-04242-](https://doi.org/10.1007/978-3-662-04242-7_8)
 892 [7_8](https://doi.org/10.1007/978-3-662-04242-7_8), 2000.
- 893 Kim, J., Dong, H. L., Seabaugh, J., Newell, S. W., and Eberl, D. D.: Role of microbes in the
 894 smectite-to-illite reaction, *Science*, 303, 830-832, <https://doi.org/10.1126/science.1093245>,
 895 2004.
- 896 Knies, J. and Martinez, P.: Organic matter sedimentation in the western Barents Sea region:
 897 Terrestrial and marine contribution based on isotopic composition and organic nitrogen
 898 content, *Norwegian Journal of Geology*, 89, 79-89, 2009.
- 899 Knight, A. W., Harvey, J. A., Shohel, M., Lu, P., Cummings, D., and Ilgen, A. G.: The combined
 900 effects of Mg²⁺ and Sr²⁺ incorporation during CaCO₃ precipitation and crystal growth,
 901 *Geochimica et Cosmochimica Acta*, 345, 16-33, <https://doi.org/10.1016/j.gca.2023.01.021>,
 902 2023.
- 903 Langrock, U., Stein, R., Lipinski, M., and Brumsack, H.-J. r.: Paleoenvironment and sea-level
 904 change in the early Cretaceous Barents Sea? implications from near-shore marine sapropels,
 905 *Geo-Marine Letters*, 23, 34-42, <https://doi.org/10.1007/s00367-003-0122-5>, 2003.
- 906 Larssen, G. B., Elvebakk, G., Henriksen, L. B., Kristensen, S.-E., Nilsson, I., Samuelsberg, T. J.,
 907 Svana, T. A., Stemmerik, L., and Worsley, D.: Upper Palaeozoic lithostratigraphy of the
 908 Southern Norwegian Barents Sea, *Norsk Geologisk Undersøkelser, Bull.*, 444, 43, 2002.
- 909 Leifer, I., Boles, J. R., Luyendyk, B. P., and Clark, J. F.: Transient discharges from marine
 910 hydrocarbon seeps: spatial and temporal variability, *Environmental Geology*, 46, 1038-1052,
 911 <https://doi.org/10.1007/s00254-004-1091-3>, 2004.
- 912 Lin, Z., Sun, X., Peckmann, J., Lu, Y., Xu, L., Strauss, H., Zhou, H., Gong, J., Lu, H., and Teichert,
 913 B. M. A.: How sulfate-driven anaerobic oxidation of methane affects the sulfur isotopic
 914 composition of pyrite: A SIMS study from the South China Sea, *Chemical Geology*, 440, 26-
 915 41, <https://doi.org/10.1016/j.chemgeo.2016.07.007>, 2016.
- 916 Mann, H. B. and Whitney, D. R.: On a Test of Whether one of Two Random Variables is
 917 Stochastically Larger than the Other, *The Annals of Mathematical Statistics*, 18, 50-60,
 918 <https://doi.org/10.1214/aoms/1177730491>, 1947.
- 919 Marín, D., Hellenen, S., Escalona, A., Olausen, S., Cedeño, A., Nøhr-Hansen, H., and Ohm, S.:
 920 The Middle Jurassic to lowermost Cretaceous in the SW Barents Sea: Interplay between

- 921 tectonics, coarse-grained sediment supply and organic matter preservation, *Basin Research*,
 922 33, 1033-1055, <https://doi.org/10.1111/bre.12504>, 2020.
- 923 Marshall, A. G. and Rodgers, R. P.: Petroleomics: the next grand challenge for chemical
 924 analysis, *Acc Chem Res*, 37, 53-59, <https://doi.org/10.1021/ar020177t>, 2004.
- 925 Matheron, G.: Principles of geostatistics, *Economic Geology*, 58, 1246-1266,
 926 <https://doi.org/10.2113/gsecongeo.58.8.1246>, 1963.
- 927 Miao, X., Feng, X., Li, J., Liu, X., Liang, J., Feng, J., Xiao, Q., Dan, X., and Wei, J.: Enrichment
 928 mechanism of trace elements in pyrite under methane seepage, *Geochemical Perspectives*
 929 *Letters*, 21, 18-22, <https://doi.org/10.7185/geochemlet.2211>, 2022.
- 930 Middelburg, J. J.: Reviews and syntheses: to the bottom of carbon processing at the
 931 seafloor, *Biogeosciences*, 15, 413-427, <https://doi.org/10.5194/bg-15-413-2018>, 2018.
- 932 Nickel, J. C., di Primio, R., Mangelsdorf, K., Stoddart, D., and Kallmeyer, J.: Characterization
 933 of microbial activity in pockmark fields of the SW-Barents Sea, *Marine Geology*, 332–334,
 934 152–162, <https://doi.org/10.1016/j.margeo.2012.02.002>, 2012.
- 935 Nickel, J. C., di Primio, R., Kallmeyer, J., Hammer, Ø., Horsfield, B., Stoddart, D., Brunstad, H.,
 936 and Mangelsdorf, K.: Tracing the origin of thermogenic hydrocarbon signals in pockmarks
 937 from the southwestern Barents Sea, *Organic Geochemistry*, 63, 73-84,
 938 <https://doi.org/10.1016/j.orggeochem.2013.08.008>, 2013.
- 939 Orphan, V. J., Hinrichs, K. U., Ussler, W., 3rd, Paull, C. K., Taylor, L. T., Sylva, S. P., Hayes, J.
 940 M., and Delong, E. F.: Comparative analysis of methane-oxidizing archaea and sulfate-
 941 reducing bacteria in anoxic marine sediments, *Appl Environ Microbiol*, 67, 1922-1934,
 942 <https://doi.org/10.1128/AEM.67.4.1922-1934.2001>, 2001.
- 943 Padilla, A. M., Loranger, S., Kinnaman, F. S., Valentine, D. L., and Weber, T. C.: Modern
 944 Assessment of Natural Hydrocarbon Gas Flux at the Coal Oil Point Seep Field, Santa Barbara,
 945 California, *Journal of Geophysical Research: Oceans*, 124, 2472-2484,
 946 <https://doi.org/10.1029/2018jc014573>, 2019.
- 947 Pearson, K.: Note on regression and inheritance in the case of two parents, *Proceedings of*
 948 *the Royal Society of London*, 58, 240-242, <https://doi.org/10.1098/rspl.1895.0041>, 1895.
- 949 Pebesma, E. J.: Multivariable geostatistics in S: the gstat package, *Computers & Geosciences*,
 950 30, 683-691, <https://doi.org/10.1016/j.cageo.2004.03.012>, 2004.
- 951 Peckmann, J., Reimer, A., Luth, U., Luth, C., Hansen, B. T., Heinicke, C., Hoefs, J., and Reitner,
 952 J.: Methane-derived carbonates and authigenic pyrite from the northwestern Black Sea,
 953 *Marine Geology*, 177, 129-150, [https://doi.org/10.1016/S0025-3227\(01\)00128-1](https://doi.org/10.1016/S0025-3227(01)00128-1), 2001.
- 954 Poetz, S., Horsfield, B., and Wilkes, H.: Maturity-Driven Generation and Transformation of
 955 Acidic Compounds in the Organic-Rich Posidonia Shale as Revealed by Electrospray
 956 Ionization Fourier Transform Ion Cyclotron Resonance Mass Spectrometry, *Energy & Fuels*,
 957 28, 4877-4888, <https://doi.org/10.1021/ef500688s>, 2014.

- 958 Pop Ristova, P., Wenzhofer, F., Ramette, A., Felden, J., and Boetius, A.: Spatial scales of
 959 bacterial community diversity at cold seeps (Eastern Mediterranean Sea), *ISME J*, 9, 1306-
 960 1318, <https://doi.org/10.1038/ismej.2014.217>, 2015.
- 961 R: A language and environment for statistical computing: <https://www.R-project.org/>, last
 962 access: 2023-06-12.
- 963 Radovic, J. R. and Silva, R. C.: Ultrahigh-Resolution Mass Spectrometry Advances for
 964 Biogeochemical Analysis: From Seafloor Sediments to Petroleum and Marine Oil Spills, *J Am
 965 Soc Mass Spectrom*, 36, 7-33, <https://doi.org/10.1021/jasms.4c00266>, 2025.
- 966 Rasheed, M. A., Lakshmi, M., Rao, P. L. S., Kalpana, M. S., Dayal, A. M., and Patil, D. J.:
 967 Geochemical evidences of trace metal anomalies for finding hydrocarbon microseepage in
 968 the petroliferous regions of the Tatipaka and Pasarlapudi areas of Krishna Godavari Basin,
 969 India, *Petroleum Science*, 10, 19-29, <https://doi.org/10.1007/s12182-013-0245-x>, 2013.
- 970 Rovere, M., Mercorella, A., Frapiccini, E., Funari, V., Spagnoli, F., Pellegrini, C., Bonetti, A. S.,
 971 Veneruso, T., Tassetti, A. N., Dell'Orso, M., Mastroianni, M., Giuliani, G., De Marco, R., Fabi,
 972 G., Ciccone, F., and Antoncicchi, I.: Geochemical and Geophysical Monitoring of
 973 Hydrocarbon Seepage in the Adriatic Sea, *Sensors (Basel)*, 20,
 974 <https://doi.org/10.3390/s20051504>, 2020.
- 975 Røy, H., Kallmeyer, J., Adhikari, R. R., Pockalny, R., Jørgensen, B. B., and D'Hondt, S.: Aerobic
 976 microbial respiration in 86-million-year-old deep-sea red clay, *Science*, 336, 922-925,
 977 <https://doi.org/10.1126/science.1219424>, 2012.
- 978 Sættem, J., Rise, L., and Westgaard, D. A.: Composition and properties of glacial
 979 sediments in the southwestern Barents Sea, *Marine Geotechnology*, 10, 229-255,
 980 <https://doi.org/10.1080/10641199109379893>, 1991.
- 981 Schippers, A. and Jørgensen, B. B.: Oxidation of pyrite and iron sulfide by manganese dioxide
 982 in marine sediments, *Geochimica et Cosmochimica Acta*, 65, 915-922,
 983 [https://doi.org/10.1016/s0016-7037\(00\)00589-5](https://doi.org/10.1016/s0016-7037(00)00589-5), 2001.
- 984 Schnabel, E., Vuillemin, A., Laczny, C. C., Kunath, B. J., Soares, A. R., Probst, A. J., Di Primio,
 985 R., Kallmeyer, J., and the, P. C.: Influence of minor hydrocarbon seepage on sulfur cycling in
 986 marine subsurface sediments, *Biogeosciences*, 22, 767-784, <https://doi.org/10.5194/bg-22-767-2025>, 2025.
- 988 Schneider, R. R., Schulz, H. D., and Hensen, C.: Marine Carbonates: Their Formation and
 989 Destruction, in: *Marine Geochemistry*, edited by: Schulz, H. D., and Zabel, M., Springer,
 990 Berlin, Heidelberg, 311-337, https://doi.org/10.1007/3-540-32144-6_9, 2006.
- 991 Schulz, H. D.: Quantification of Early Diagenesis: Dissolved Constituents in Pore Water and
 992 Signals in the Solid Phase, in: *Marine Geochemistry*, 73-124, https://doi.org/10.1007/3-540-32144-6_3, 2006.
- 994 Sedgwick, P.: Pearson's correlation coefficient, *Bmj*, 345, e4483-e4483,
 995 <https://doi.org/10.1136/bmj.e4483>, 2012.

- 996 Seeberg-Elverfeldt, J., Schluter, M., Feseker, T., and Kolling, M.: Rhizon sampling of
 997 porewaters near the sediment-water interface of aquatic systems, *Limnol Oceanogr-Meth*,
 998 3, 361-371, <https://doi.org/10.4319/lom.2005.3.361>, 2005.
- 999 Sert, M. F., D'Andrilli, J., Gründger, F., Niemann, H., Granskog, M. A., Pavlov, A. K., Ferré, B.,
 1000 and Silyakova, A.: Compositional Differences in Dissolved Organic Matter Between Arctic
 1001 Cold Seeps Versus Non-Seep Sites at the Svalbard Continental Margin and the Barents Sea,
 1002 *Frontiers in Earth Science*, 8, <https://doi.org/10.3389/feart.2020.552731>, 2020.
- 1003 Siegert, M. J., Dowdeswell, J. A., Hald, M., and Svendsen, J. I.: Modelling the Eurasian Ice
 1004 Sheet through a full (Weichselian) glacial cycle, *Global and Planetary Change*, 31, 367-385,
 1005 [https://doi.org/10.1016/S0921-8181\(01\)00130-8](https://doi.org/10.1016/S0921-8181(01)00130-8), 2001.
- 1006 Smrzka, D., Lin, Z., Monien, P., Chen, T., Bach, W., Peckmann, J., and Bohrmann, G.: Pyrite-
 1007 based trace element fingerprints for methane and oil seepage, *Geochemical Perspectives*
 1008 *Letters*, 29, 33-37, <https://doi.org/10.7185/geochemlet.2409>, 2024.
- 1009 Smrzka, D., Zwicker, J., Bach, W., Feng, D., Himmler, T., Chen, D., and Peckmann, J.: The
 1010 behavior of trace elements in seawater, sedimentary pore water, and their incorporation
 1011 into carbonate minerals: a review, *Facies*, 65, 47, [https://doi.org/10.1007/s10347-019-0581-](https://doi.org/10.1007/s10347-019-0581-4)
 1012 4, 2019.
- 1013 Smrzka, D., Feng, D., Himmler, T., Zwicker, J., Hu, Y., Monien, P., Tribovillard, N., Chen, D.,
 1014 and Peckmann, J.: Trace elements in methane-seep carbonates: Potentials, limitations, and
 1015 perspectives, *Earth-Science Reviews*, 208, <https://doi.org/10.1016/j.earscirev.2020.103263>,
 1016 2020.
- 1017 Tribovillard, N., du Châtelet, E. A., Gay, A., Barbecot, F., Sansjofre, P., and Potdevin, J.-L.:
 1018 Geochemistry of cold seepage-impacted sediments: Per-ascensum or per-descensum trace
 1019 metal enrichment?, *Chemical Geology*, 340, 1-12,
 1020 <https://doi.org/10.1016/j.chemgeo.2012.12.012>, 2013.
- 1021 Viollier, E., Inglett, P. W., Hunter, K., Roychoudhury, A. N., and Van Cappellen, P.: The
 1022 ferrozine method revisited: Fe(II)/Fe(III) determination in natural waters, *Applied*
 1023 *Geochemistry*, 15, 785-790, [https://doi.org/10.1016/s0883-2927\(99\)00097-9](https://doi.org/10.1016/s0883-2927(99)00097-9), 2000.
- 1024 von Breyman, M. T., Brumsack, H., and Emeis, K. C.: Depositional and Diagenetic Behavior
 1025 of Barium in the Japan Sea, in: *Proceedings of the Ocean Drilling Program, 127/128 Part 1*
 1026 *Scientific Results, Proceedings of the Ocean Drilling Program*,
 1027 <https://doi.org/10.2973/odp.proc.sr.127128-1.168.1992>, 1992.
- 1028 Vuillemin, A., Morlock, M., Paskin, A., Benning, L. G., Henny, C., Kallmeyer, J., Russell, J. M.,
 1029 and Vogel, H.: Authigenic minerals reflect microbial control on pore waters in a ferruginous
 1030 analogue, *Geochemical Perspectives Letters*, 28, 20-26,
 1031 <https://doi.org/10.7185/geochemlet.2339>, 2023a.

- 1032 Vuillemin, A., Vargas, S., Coskun, O. K., Pockalny, R., Murray, R. W., Smith, D. C., D'Hondt, S.,
1033 and Orsi, W. D.: Atribacteria Reproducing over Millions of Years in the Atlantic Abyssal
1034 Subseafloor, *mBio*, 11, <https://doi.org/10.1128/mBio.01937-20>, 2020.
- 1035 Vuillemin, A., Mayr, C., Schuessler, J. A., Friese, A., Bauer, K. W., Lücke, A., Heuer, V. B.,
1036 Glombitza, C., Henny, C., von Blanckenburg, F., Russell, J. M., Bijaksana, S., Vogel, H., Crowe,
1037 S. A., and Kallmeyer, J.: A one-million-year isotope record from siderites formed in modern
1038 ferruginous sediments, *GSA Bulletin*, 135, 504-522, <https://doi.org/10.1130/b36211.1>,
1039 2023b.
- 1040 Wickham, H.: *ggplot2, 2, Use R!*, Springer-Verlag, New York, 260 pp.,
1041 <https://doi.org/10.1007/978-3-319-24277-4>, 2016.
- 1042 Widdel, F., Knittel, K., and Galushko, A.: Anaerobic Hydrocarbon- Degrading
1043 Microorganisms: An Overview, in: *Handbook of Hydrocarbon and Lipid Microbiology*,
1044 Springer, Berlin, Heidelberg, 1997-2021, <https://doi.org/10.1007/978-3-540-77587-4>, 2010.
- 1045 Yergin, D.: *The Prize: The Epic Quest for Oil, Money & Power*, Free Press, ISBN
1046 9781847376466, 2009.
- 1047 Zhang, X., Wu, K., Han, Z., Chen, Z., Liu, Z., Sun, Z., Shao, L., Zhao, Z., and Zhou, L.: Microbial
1048 diversity and biogeochemical cycling potential in deep-sea sediments associated with
1049 seamount, trench, and cold seep ecosystems, *Front Microbiol*, 13, 1029564,
1050 <https://doi.org/10.3389/fmicb.2022.1029564>, 2022.
- 1051 Zhao, R. X., Xue, H. T., Lu, S. F., Greenwell, and Erastova, V.: Revealing crucial effects of
1052 reservoir environment and hydrocarbon fractions on fluid behavior in kaolinite pores, *Chem
1053 Eng J*, 489, <https://doi.org/10.1016/j.cej.2024.151362>, 2024.